A 3D Shear Velocity Model of the Crust and Uppermost Mantle Beneath the United States from Ambient Seismic Noise

G. D. Bensen

Center for Imaging the Earth's Interior, Department of Physics, University of Colorado at Boulder, Boulder, Colorado USA

M. H. Ritzwoller

Center for Imaging the Earth's Interior, Department of Physics, University of Colorado at Boulder, Boulder, Colorado USA

Y. Yang

Center for Imaging the Earth's Interior, Department of Physics, University of Colorado at Boulder, Boulder, Colorado USA

G. D. Bensen, Department of Physics, University of Colorado at Boulder, Campus Box 390, Boulder, CO 80309, USA. (gbensen@colorado.edu)

Abstract.

Recent work in ambient noise surface wave tomography has shown that high resolution dispersion maps can be obtained reliably in a wide variety of settings. *Bensen et al.* [2007b] used 203 stations across North America to produce nearly 9,000 dispersion curves after measurement selection, creating Rayleigh and Love wave dispersion maps from 8 - 70 s period and 8 - 20 s period, respectively, on a 0.5° x 0.5° grid. These maps, produce Rayleigh and Love wave group and phase speed dispersion curves at each grid point which we invert through a two-step procedure to determine a three-dimensional (3D) shear wave velocity model of the crust and uppermost mantle beneath much of North America. The first step is a linearized inversion for the best fitting model. This is followed by a Monte-Carlo inversion to estimate model uncertainty. In general, a simple model parameterization is sufficient to achieve acceptable data fit, but the problem of isotropic model dispersion underestimating Love wave speed and overestimating Rayleigh wave speed is common. This observation is particularly pronounced in areas that have experienced extension, which can induce flow causing radial anisotropy. Data fit improves by allowing alternative parameterizations of radial anisotropy or low velocity zones in the middle and lower crust. Crustal features observed in the model include sedimentary basins such as the Anadarko, Green River, Williston Basins as well as the Great Valley and the Mississippi Embayment. An abrupt crustal velocity transition is seen from the Rocky Mountains to the Great Plains. Differing degrees of homogeneity in crustal velocity are also

observed. Recovered crustal thickness is similar to the Crust 2.0 model of *Bassin et al.* [2000]. Examples of Airy and Pratt compensation are seen below the Great Plains and Basin and Range respectively. The mantle wedge below Cascadia, a clearer outline of the North American Craton and the strong signal from the Northern Basin and Range are among the mantle features imaged.

1. Introduction

Seismic tomographic investigations on both global and regional scales have been performed covering all or part of the continental United States. However, the resulting models have had either limited geographic extent or relatively low resolution. Previous studies also have shown that surface wave ambient noise tomography (ANT) helps to fill the gap between regional and continental/global scale tomographic models (e.g., *Moschetti et al.* [2007], *Lin et al.* [2007], *Yang et al.* [2007], *Yao et al.* [2006]). Still, the full potential of the bandwidth and, therefore, the depth extent of ANT remains untested. In addition, little work exists towards a 3D inversion of ANT results using Rayleigh and Love wave group and phase speed measurements. Employing these techniques, we show that ANT effectively diminishes the typical resolution/coverage trade-off and provides higher resolution results across the continental US than achieved by previous studies on this scale. Seismic data now emerging from Earthscope's USArray provide the potential for further improvement in resolution for which our model may serve as a useful reference.

This study is an extension of work presented by *Bensen et al.* [2007a] and *Bensen et al.* [2007b]. *Bensen et al.* [2007a] presented a technique for computing reliable empirical Green functions (EGF) from long sequences of ambient noise. They also presented an automated procedure to measure the dispersion of EGFs as well as selection criteria to ensure that only high-quality signals are retained. Using these methods, *Bensen et al.* [2007b] estimated maps of Rayleigh and Love wave group and phase speed across the study region presented in Figure 1. Using 203 stations across North America (labeled as black triangles in Figure 1) for up to two years of ambient noise data, they developed surface wave dispersion maps across the study region on a 0.5° x 0.5° grid. They constructed dispersion maps from 8 - 70 s period for Rayleigh waves and 8 - 20 s period for Love waves. These dispersion maps form the basis for the current study. Additionally, *Bensen et al.* [2007b] presented evidence building credibility in the ANT technique, as well as empirical information about the nature of the distribution of ambient seismic noise. Aspects of the work by *Bensen et al.* [2007a] and *Bensen et al.* [2007b] are summarized here as appropriate.

Regional investigations of surface wave propagation and dispersion in the United States date back over 30 years (e.g., *Lee and Solomon* [1978]). Tomographic studies using data in the United States (e.g., *Alsina et al.* [1996], *van der Lee and Nolet* [1997], *Godey et al.* [2003], *Li et al.* [2003], *Marone et al.* [2007]) created dispersion maps and models covering our study area, which possess resolution similar to global scale studies (e.g., *Trampert and Woodhouse* [1996], *Ekström et al.* [1997], *Ritzwoller et al.* [2002]).

In addition, a large number of smaller-scale regional studies have been performed to investigate the seismic structure of North America. Among these are tomographic studies in regions such as the Rio Grande Rift (e.g., *Gao et al.* [2004]), Cascadia (e.g., *Ramachandran et al.* [2005]), California (e.g., *Thurber et al.* [2006]), the Rocky Mountains (e.g., *Yuan and Dueker* [2005]) and the eastern US (e.g., *van der Lee* [2002]) just to name a few recent studies among many others. Many refraction studies have provided profiles across North America, including CD-ROM (e.g., *Karlstrom et al.* [2002]), Deep Probe (e.g., *Snelson et al.* [1998]) and others. Receiver functions have provided valuable constraints on crustal thickness and structure through much of the continent (e.g., *Crotwell and Owens* [2005]). However, compiling and integrating regional results together into a single high-resolution model with broad coverage is a difficult task considering the variety of techniques and differences in resolution among them.

ANT presents several advantages over previously used techniques. First, higher seismic ray path density is achieved and these paths are contained entirely within the study region, creating a more nearly optimal configuration for tomographic inversion. Second, station locations are precisely known unlike earthquake locations. Third, new empirical observations have clarified the phase content of ambient noise for phase velocity measurements (*Lin et al.* [2007]) reducing ambiguity and facilitating high measurement precision compared to earthquake observations. Fourth, *Bensen et al.* [2007b] computed multiple, seasonally variable EGFs along each path in order to quantify measurement variability which has been impossible with previous studies. Fifth, the bandwidth of ambient noise derived measurements (i.e., 6 - 100 s period) constrains the structure both of the crust and uppermost mantle. In contrast, it is difficult across much of the US to obtain high-quality earthquake based surface wave dispersion measurements below ∼15 s period. Despite good lateral coverage, many previous surface wave studies have obtained high-quality dispersion measurements only at longer periods and, therefore, reported velocity structure only in the mantle (e.g., *Shapiro and Ritzwoller* [2002], *van der Lee and Frederiksen* [2005]). Similarly, body wave studies of similar geographic extent provide only weak constraints on crustal structure(e.g., *Grand* [1994], *Grand* [2002]). Accordingly, *Bensen et al.* [2007b] reported an increase in lateral resolution by about a factor of 5 (i.e., 200 km versus 1000 km) compared to previous earthquake based surface wave investigations of similar spatial scale.

The 3D model derived from this work will be useful to improve earthquake locations in some regions, aid receiver function studies, and provide a starting model for a wide variety of investigations across the US. This may be especially important in the context of the advancing USArray/Transportable Array experiment. Velocity models are also important tools for guiding tectonic inferences. Even by compiling multiple models one falls short of linking the unique tectonic provinces of North America into a coherent integrated model. Furthermore, less seismically active regions of North America, such as the central plains and the eastern United States, are harder to constrain seismically than the tectonically active western US. In some areas, the model presented herein will be the highest resolution model available.

The current study uses a two-step procedure to create a 1D velocity model at each point on a 0.5° x 0.5° grid based on the dispersion maps of *Bensen et al.* [2007b]. The first step is a linearized inversion for an isotropic shear velocity profile from the set of dispersion curves at each grid point. The inversion is inherently non-unique and a variety of models of varying levels of complexity can be created that fit the data within the data uncertainty. In the second step of the inversion, in order to quantify the level with which we can trust the results of the inversion, we perform a Monte-Carlo re-sampling of model space near to the best fitting model derived from the linearized inversion, to develop an ensemble of models at each grid point that fit the data acceptably. From this we quantify the model uncertainty and choose a "favored model" near the center of the distribution to represent the ensemble. The final model is, therefore, a 3D volume of isotropic shear wave velocity and uncertainty at each point in the area of good resolution outlined in Figure 2. The vertical extent of the model is from the surface to about 150 km depth.

2. Data

The data used in this study are Rayleigh and Love wave group and phase speed dispersion maps of *Bensen et al.* [2007b]. These maps are based on Rayleigh and Love wave group and phase speed dispersion measurements obtained from EGFs computed along paths between the stations shown in Figure 1. Dispersion measurements are made on EGFs created by cross-correlating long ambient noise time series using the data processing and measurement techniques described in detail by *Bensen et al.* [2007a] and *Lin et al.* [2007]. Nearly 20,000 paths are used for this experiment and up to 13 unique measurements from different temporal subsets along each path are computed for the uncertainty analysis. An automated Frequency Time Analysis (FTAN) is necessary to measure the dispersion of these Rayleigh and Love wave signals. The seminal description of the FTAN procedure can be found in *Levshin et al.* [1972] and details of our automated procedure are outlined by *Bensen et al.* [2007a].

Bensen et al. [2007b] developed acceptance criteria to ensure that only signals of sufficient quality are retained. In short, starting with nearly 20,000 paths across the United States and Canada, a maximum of 8,932 paths remained after rejection. The rejection procedure consists of three parts. The first is a minimum signal-to-noise ratio (SNR) criterion. Secondly, EGFs for different 6-month time intervals of ambient noise are computed, yielding a set of temporally variable EGFs for each path. Observations with little variability in the repeated dispersion measurements are retained. Finally, data with large time residuals after an initial overly smooth tomographic inversion are rejected. *Bensen et al.* [2007b] inverted the selected dispersion measurements using a linear tomographic inversion described in detail by *Barmin et al.* [2001] (an abbreviated introduction is presented by *Bensen et al.* [2007b]) to generate group and phase speed tomography maps for Rayleigh waves between 8 and 70 s period and between 8 and 20 s for Love waves. Low signal quality for Love waves at longer periods causes the narrower bandwidth and apparently results from higher local noise on horizontal components. Selected examples of these maps and discussion of their quality is presented by *Bensen et al.* [2007b]. Additionally, selected Rayleigh and Love wave group and phase speed dispersion maps can be found at *http : //ciei.colorado.edu/∼gbensen/dispersion_maps.html*. The resulting bandwidth presents a depth sensitivity from the surface into the upper mantle, as seen in Figure 3. Our study has better shallow depth sensitivity than previous studies of similar geographic scale due to the shorter period measurements that derive from ambient noise.

Starting with the set of Rayleigh and Love wave group and phase speed dispersion maps at different periods, dispersion curves are constructed for at each point on the $0.5°$ x $0.5°$ grid across the US. This process is similar to many previous studies such as *Ritzwoller and Levshin* [1998], *Villaseñor et al.* [2001], *Shapiro and Ritzwoller* [2002], *Weeraratne et al.* [2003], and others. For all periods, at each geographic point, it is important to assign an uncertainty value within which the modeled dispersion curve should lie. *Shapiro and Ritzwoller* [2002] assigned uncertainty at each point as the RMS tomography misfit weighted by resolution, which was effective for their global scale work. Given that crustal anomalies are often greater in magnitude than mantle anomalies, we favor a different approach. Changing the regularization of the tomographic inversion can affect the exact location, extent and amplitude of velocity anomalies appreciably. These changes in the recovered anomalies, due to subjective decisions, are a source of ambiguity in the tomographic results. To address this, we create a set of reasonable dispersion maps for each period and wave type by using a range of regularization parameters. The minimum and maximum velocity at each point for each period define an uncertainty window for that wave type. We find that regions of greatest variability occur near significant velocity anomalies and near the edges of the study area. We set a minimum uncertainty value for Rayleigh wave group and phase speed at 20 and 30 m/s, respectively. Love wave phase speed minimum uncertainty is set at 30 m/s. We do not use Love wave group speed dispersion curves in this study because of lower confidence in their robustness. Finally, we weight the uncertainty values by the estimated resolution. The weighting factor is unity for grid points with resolution of 400 km or better. The uncertainty at grid points with lower resolution is weighted higher to a maximum allowed measurement uncertainty of 100 m/s. For reference, the 500 km resolution contour for the 16 s Rayleigh wave phase speed map is shown in Figure 2; resolution of other maps is generally no better than this. The mean uncertainty over all periods for the measurements used in this study is shown in Figure 4. Rayleigh wave uncertainty increases appreciably near the extremes of the period band. By comparison, the uncertainty values we used are smaller than RMS tomography misfit values from *Bensen et al.* [2007b] at all periods for all wave types. The uncertainties change across the US from 20 - 100 m/s for Rayleigh phase velocity maps and from 30 - 100 m/s for Rayleigh group and Love phase velocity maps.

3. Methods

Two commonly used methods exist for obtaining shear wave velocity structure from surface wave dispersion measurements. The first is a linearized waveform fitting as described by *Snieder* [1988], *Nolet* [1990] and others. This technique has been used in many geographical settings with earthquake surface wave signals, including the US (*van der Lee* *and Nolet* [1997]). The second method, which we adopt, is a two-stage procedure in which period specific 2D tomographic maps created from the dispersion measurements are used to produce dispersion curves at each geographic grid point. The dispersion curves are then inverted for 1D *Vs* structure at all grid points and the 1D models are compiled to obtain a 3D volume. This procedure has been described by *Shapiro and Ritzwoller* [2002] and elsewhere.

The specific approach we take divides into two further steps. The first step is a linearized inversion of the dispersion curves for the 1D velocity structure at each point. However, the best fitting model does not account for the non-uniqueness of the inverse problem; a variety of acceptable models may be created that fit the data with the desired accuracy. In the second step, for this reason, we perform a Monte-Carlo search of a corridor of model space defined by the results of the linearized inversion. From this we define an ensemble of velocity models that fit the data acceptably. In contrast, a Monte-Carlo search of a broader model space, which is not constrained by the results of the linearized inversion, is much slower. These two steps are outlined further below. The linearized inversion procedure only uses Rayleigh and Love wave phase speed measurements while Rayleigh wave group speed measurements are also included in the Monte-Carlo procedure.

3.1. Starting Models and Parameterization

Both the linearized inversion and the Monte-Carlo sampling require a starting model. Previous work used AK135 (*Kennett et al.* [1995]) as a starting model for all points (see *Weeraratne et al.* [2003]). For the linearized inversion, we observe faster and more stable convergence by using unique starting models at each geographic point. For this, we extract shear wave speed values from *Shapiro and Ritzwoller* [2002]. The procedure also requires values of P-wave speed (Vp) and density (ρ). We use the average continental Vp/Vs ratios of 1.735 in the crust and 1.756 in the mantle from *Chulick and Mooney* [2002] who found little deviation from these value across the US. Furthermore, surface waves are less sensitive to Vp than Vs except in the uppermost crust. Density (ρ) is assigned similarly using a ρ/Vs ratio of 0.81 as described by *Christensen and Mooney* [1995]. Following previous work (i.e., *Weeraratne et al.* [2003]), we parameterize the models with 18 layers. Three crustal layers are used where the top layer thickness is set at the greater of 2 km or the sediment thickness from the model of *Laske and Masters* [1997]. The depth to the Moho was extracted from *Bassin et al.* [2000]. These two inputs define a thin upper crustal layer and a thick middle to lower crustal layer. The lower crustal layer was separated into two layers of equal thickness defining the middle and lower crust. The 15 layers in the mantle are between 20 and 50 km thick and extend to 410 km depth. An illustration of the parameterization is shown in Figure 5a. In the linearized inversion, the velocities of all layers are allowed to change although regularization is applied to ensure smoothness, as discussed in Section 3.2 below. Vp/Vs and ρ/Vs are maintained at the values stated above. Finally, only the thicknesses of the lower crust and uppermost mantle are permitted to change. However, if poor data fit is observed, we perturb the upper and middle crustal layer thicknesses (while maintaining the initial crustal thickness) and the inversion is rerun.

For Monte-Carlo sampling we use the result of the linearized inversion as a starting model. However, we also impose an explicit requirement of monotonically increasing crustal velocity with depth. Within our study area, *Wilson et al.* [2003] and *Ozalaybey et al.* [1997] found evidence for low-velocity zones (LVZ) in the crust from localized magma bodies and regional partial melt, respectively. Using receiver functions and surface wave dispersion to constrain the crust, *Ozalaybey et al.* [1997] allowed ~20 crustal layers. At a variety of locations, their crustal LVZ was often 5 km or less in thickness. These crustal LVZs and other similar features documented in the literature are of insufficient vertical and/or lateral extent for us to image reliably. Furthermore, a model parameterization using isotropic crustal velocities still produces good data fit. In contrast, *Ozalaybey et al.* [1997] find evidence for an upper mantle LVZ in northwestern Nevada, which is permitted in our mantle parameterization. In the mantle, Monte-Carlo sampling of 15 layers, as used in the linearized inversion, is costly and would potentially create unrealistic models or require the additional complexity of a smoothing regularization. For speed and smoothness, we parameterize the mantle with five B-splines. An illustration of this model parameterization of the model is shown in Figure 5b.

From the linearized inversion described above, we obtain smooth, simple 1D velocity profiles at all grid points in the study area which typically fit the data remarkably well. For the Monte-Carlo sampling we define the allowed range of models based on this best fitting result. First, we impose a constraint on the permitted excursions from the initial velocity values. The velocity must be within ± 20% of the initial model in the upper crust and ± 10% in the lower crust and mantle. We chose this range rather than a specific velocity window (e.g., ± 0.5 km/s) because of the potential for unrealistically low values in the crust. By comparison, our allowed corridor is wider than *Shapiro and Ritzwoller* [2002]. Again, we maintain the Vp/Vs and Vs/ρ values stated above. However, the thicknesses of the crustal layers can now vary while the sum of crustal layers must be within ± 5 km from the Crust 2.0 model of *Bassin et al.* [2000].

Complexities probably exist within the crust and upper mantle that may not be well represented by our simple parameterization. However, if data fit is reasonable, we cannot empirically justify a more complicated model without inclusion of independent information such as receiver functions. The non-uniform coverage of receiver functions would make this particular exercise difficult on our scale.

3.2. Linearized Inversion

The linearized inversion process uses a starting model to create predicted dispersion curves. Perturbing the input model provides misfit information and iterating converges upon the best-fitting solution. The linearized inversion process follows the work of *Li et al.* [2003], *Weeraratne et al.* [2003], *Forsyth and Li* [2005] and others. In this case, the forward code used to compute dispersion curves from an input model is based on sai.

The technique to find the best fitting velocity model is outlined by *Weeraratne et al.* [2003] and is based on the iterative least-squares approach of *Tarantola and Valette* [1982]. *Li et al.* [2003] concisely summarize the approach, which we excerpt here. The solution is described by the equation:

$$\mathbf{\Delta m} = (\mathbf{G}^T \mathbf{C}_{nn}^{-1} \mathbf{G} + \mathbf{C}_{mm}^{-1})^{-1} (\mathbf{G}^T \mathbf{C}_{nn}^{-1} \mathbf{\Delta d} - \mathbf{C}_{mm}^{-1} [\mathbf{m} - \mathbf{m_0}]) \qquad (1)$$

where $\mathbf{m}$ is the current model, $\mathbf{m_0}$ is the starting model at the outset of each iteration, and $\mathbf{\Delta m}$ is the change to the model. $\mathbf{\Delta d}$ is the difference between the observed and predicted data. $\mathbf{G}$ is a sensitivity matrix relating changes in $\mathbf{d}$ to changes in $\mathbf{m}$. $\mathbf{C_{mm}}$ is the model covariance matrix where non-zero values (we use 0.l) are introduced into the off-diagonal terms in order to provide a degree of correlation between velocity values obtained for each layer and its neighbors and ensure a reasonable model (i.e., a model without large velocity jumps or oscillations). $\mathbf{C_{nn}}$ is the data covariance matrix where the diagonal elements are calculated from the standard errors of the phase velocities and the off-diagonal elements are assumed to be 0.

As a measure of data fit quality, we use reduced χ^2 (henceforth χ^2). Unique χ^2 values are computed for Rayleigh wave and Love wave phase speed; χ^2 is also computed for Rayleigh wave group speed in the Monte-Carlo re-sampling described below. χ^2 is defined as

$$\chi^2 = \frac{1}{n}\sum_{i=1}^{n} \frac{(\tilde{d}_i - d_i)^2}{\delta_i^2} \tag{2}$$

where i is the index of the period of the measurement through all wavetypes used. Periods used are on a 2 second grid from 8 - 20 s period and every 5 seconds for 25 - 70 s period. Therefore, n is 7 for Love waves and 17 for Rayleigh waves. Thus, in the linearized inversion, 24 measurements are used but in the Monte-Carlo inversion, 41 measurements are applied because Rayleigh wave group speeds are utilized. $\tilde{d}$ and d_i are the model predicted and measured wave speeds, respectively and δ_i is the uncertainty of the measured velocity unique to each period, wave type and location, as described in Section 2 above. χ^2 is a metric indicating how well the model prediction fits the data within estimated uncertainty values. A χ^2 value less than or equal to unity indicates a fit within the estimated uncertainty of the data. Generally, χ^2 values of 2 or less represent good data fit. Higher values indicate inferior fit or underestimated data uncertainties.

An example of input data and model output from the linearized inversion is shown in Figure 6 for a point in Illinois. For reference, the location of this point is plotted as a grey circle in Figure 1. Dispersion observations and associated errors are plotted as error bars in Figure 6a. The resulting best fitting models and related dispersion curves produced by linearized inversion are shown as thin black lines in Figure 6b. For comparison, the starting model and the related dispersion curves are shown in Figure 6 as dotted grey lines.

Variability in data fit quality is present in the study area. Figure 7 shows two more examples like Figure 6 with higher resulting χ^2 values. Considering that the location of data used in Figure 7c,d is in an area of particularly good resolution (southern California), the misfit likely derives from improper model parameterization. In this case, the short period under-prediction of Love wave speeds and over-prediction of Rayleigh wave speeds may indicate the need for radial anisotropy in the crust. More discussion alternative parameterizations follows in Section 6.3. For reference, the approximate depth sensitivity of Rayleigh and Love phase velocity at selected periods are shown in Figure 3. Examination of these sensitivity plots confirms that higher misfit (e.g., Figure 7a) could be due to improper model parameterization at depths from 0 - 30 km.

3.3. Monte-Carlo Re-sampling and Uncertainty Estimation

To estimate uncertainties in geophysical inverse problems, Monte-Carlo methods have been in use for over 40 years (*Keilis-Borok and Yanovskaya* [1967]) and can provide reliable uncertainty estimates even when the *a priori* probability density of solutions is unknown (see *Mosegaard and Tarantola* [1995]). Variations among Monte-Carlo methods are summarized by *Sambridge and Mosegaard* [2002]. Methods to sample model space more effectively and/or more quickly are presented therein. One particular concern in our inverse problem is the tradeoff between velocity values in the lower crust and uppermost mantle with crustal thickness. This is considered a significant problem by *Marone and Romanowicz* [2007] and elsewhere provides part of the motivation for us to estimate model uncertainty. We quantify the variation of acceptable models and use this variation as an indication of the robustness of the resulting velocity model.

The Monte-Carlo procedure we employ is a two-step procedure that first creates models through uniformly distributed random perturbations within the permitted corridor around the model provided by linearized inversion, as described above. Secondly, a random walk is used to refine the search for acceptable models. Rayleigh wave group and phase and Love wave phase speed dispersion curves are generated for each model using the forward code of *Herrmann* [1987]. If the predicted dispersion curves match the measured results at an acceptable level, the model is retained. An acceptable model is defined as one having a χ^2 value within 3 times the χ^2 value obtained from the linearized inversion. For Rayleigh group velocity values, the χ^2 limit is 6 times the Rayleigh wave phase velocity best fit value. In order to accelerate the process of obtaining a sufficient number of acceptable models, we employ a random walk procedure generates small perturbations to search adjacent model space for additional acceptable models. After the random walk identifies an acceptable model, the search re-initializes in the neighborhood of that model until a level of convergence is observed. After convergence, we return to the first step of a uniform search of all permitted model space.

An example of the input dispersion curves and the Monte-Carlo results are shown in Figure 8 for points labeled as grey squares in Figure 1. The model ensembles in the examples presented display the strongest variability at different depths while all have similar variability in the resulting dispersion curves. Thus, the goodness of fit for a computed dispersion curve is not necessarily a clear indicator of a robust model.

We select a “favored model” from the set of resulting velocity models. The best-fitting model is very similar to that determined through linearized inversion and may not capture the essence of the ensemble of models very well. We favor the model closest to the mean of the distribution, where greater depths are given lesser precedence. This captures the essence of the ensemble and diminishes the occasional problems of lateral roughness found when only the best fitting velocity models are considered. For illustration, the models most near the mean of the distribution are plotted in red in Figure 8a,c,e and are henceforth referred to as the “favored models”. Further discussion of model variability across the study area is reserved for Section 5 below.

4. Crustal Rayleigh/Love Wave Speed Discrepancy

The observation of lower data fit in regions of good resolution deserves further comment. The distributions of χ^2 values for Rayleigh and Love wave phase speeds separately are shown in Figure 9. Because the solution procedure attempts to minimize data misfit for Rayleigh and Love waves simultaneously, the observation that areas of high χ^2 for Rayleigh and Love waves approximately coincide is no surprise. The primary cause for larger misfit may be attributed to three factors. The first factor is that the data error estimates that we used could be too low and in fact our confidence in the input dispersion maps is overestimated. This may be the case along the edges of the experiment. Secondly, higher misfit may also occur when the results for different wave types have incompatible resolutions, causing velocity transitions to manifest themselves in different locations for different wave types. The third factor is that our simple model parameterization insufficiently describes the earth at a given point. Poorer agreement in the data primarily at short periods suggests that the deficiency in parameterization would be in the crust.

A three-layer crust and multi-layer mantle can usually fit either Rayleigh or Love wave measurements satisfactorily. However, fitting data to both simultaneously is more difficult. Figure 10 shows the difference in misfit to Rayleigh and Love waves phase velocities across the US. We compute the difference between the isotropic "favored model" minus the input dispersion map at each point and divide this by the estimated data error. These values are averaged from 8 - 20 s period. Green, yellow and red colors indicate the the model is faster than an observation at a point. Blue to violet colors indicate that the model is too slow to fit the observations. The widespread result of Rayleigh and Love wave speeds being over- and under-predicted, respectively, is apparent. The period band (8 - 20 s) indicates that the source of this discrepancy lies in the crust. We, therefore, refer to this as the crustal Rayleigh/Love discrepancy to distinguish it from the well known mantle Rayleigh/Love discrepancy caused by radial anisotropy in the mantle (e.g., *Dziewonski and Anderson* [1981]). Section 6.3 below discusses possible causes of this observation and our preferred explanation.

5. Results

As discussed above, we construct a "favored model" from an ensemble of models that fit the data acceptably, developed through Monte-Carlo inversion at each grid point. Compiling these 1D isotropic models, we obtain a 3D shear wave velocity model for the continental US with lateral coverage bounded approximately by the black contour in Figure 2 and depth range from the surface to 150 km. Here, we characterize the model by highlighting examples of the types of features it contains. The names of features listed in Figure 2 are used in this discussion.

Slices of isotropic shear wave speed at a selection of depths are shown in Figure 11 including 4 km above (Figure 11c) and 4 km below (Figure 11d) the recovered Moho. For plotting purposes, we smooth the model features and soften the abrupt contrasts between layers, by vertically averaging in 5 km increments in the crust and 10 km in the mantle. Thus, a depth section at 10 km is the average from 8 - 12 km depth. No smoothing is applied across the Moho.

The most striking features at 4 km depth (Figure 11a) are several large sedimentary basins. The Mississippi Embayment and the Green River Basin appear most strongly. Additionally, the Williston Basin and Anadarko Basin in Montana and Oklahoma, respectively, clearly appear as slow velocity anomalies. Low velocities associated with the sediments of the Great Valley in California abut slow crustal velocities of the Cenozoic volcanic Columbia Plateau farther north. The trend of generally faster velocities in the eastern US is also observed.

At a depth of 10 km (Figure 11b), the most pronounced feature is again the strong signal from the deep sediments of the Mississippi Embayment, which have been extended to this depth by the vertical averaging. The crustal velocity dichotomy observed at 4 km depth between the faster eastern US and slower western US continues to be clearly defined. The crustal velocity dichotomy at this depth is located along the boundary between the Great Plains and Central Lowlands and will be discussed in detail in Section 6.1 below. This middle crustal east-west velocity dichotomy is an example of a feature that was too thin to be resolved by previous continental scale surface wave studies.

Moving to the lower crust, Figure 11c at 4 km above the Moho shows a different location of the crustal velocity dichotomy in the central US, shifted west to coincide with the transition from the Great Plains to the Rocky Mountain Front. Also, the slow anomaly in the Basin and Range can be attributed to high crustal temperatures in this extensional province, as evidenced by high surface heat flow in the area (see e.g., *Blackwell et al.* [1990]). The fast anomaly in the Great Lakes area may result from regionally thicker crust; a slice at 4 km above the Moho is at greater depths than the surrounding region. However, slower speeds beneath the Appalachian Highlands to the east has similarly thick crust, implying that compositional differences between the Appalachian Highlands and the continental shield are the more likely cause of this velocity anomaly. For reference, the estimated crustal thickness is shown in Figure 12 and is discussed below.

At 4 km below the Moho (Figure 11d), the east-west velocity dichotomy is in a similar location as in the lower crust. This will be discussed at greater length in Section 6.1 below. East of this transition, more laterally homogenous mantle velocities appear. In the west, the prominent slow anomaly below the eastern Basin and Range is striking and corroborates the suggested removal of mantle lithosphere from 10 Ma to present (e.g., *Jones et al.* [1994]) and replacement with warmer, low velocity mantle material. The slow anomaly in the Pacific Northwest can be attributed to the volatilized mantle wedge residing above the subducting slab. At 80 km depth (Figure 11e), however, the slow anomaly associated with the mantle wedge is no longer visible, suggesting that this depth is below or within the subducting slab. Also, a slow mantle velocity anomaly extends in the northwest to southeast direction, roughly following the outline of the entire Basin and Range province. This feature was also observed in the tomographic model of *Alsina et al.* [1996] and has been attributed to inflow of warm mantle material during Cenozoic extension (e.g., *Wernicke et al.* [1988]). At 120 km depth in Figure 11f, features are similar to 80 km depth, but anomalies are of lower amplitude.

The estimated crustal thickness is similar to the starting model of Crust 2.0 (*Bassin et al.* [2000]) and is shown in Figure 12. On average, the crust is 1.6 km thinner than Crust 2.0 and the RMS difference from Crust 2.0 across the study region is 1.5 km. These differences are not strongly concentrated in any specific regions where the Monte-Carlo ensemble suggests a significant offset from the Crust 2.0. The relation of crustal thickness with topography and implications for topographic compensation are discussed after the following paragraph.

Vertical cross-sections through the velocity model on a 0.5° grid reveal more information about the structure of the study area. Figure 13 presents a series of vertical cross-sections with locations indicated on the map in Figure 13a. A smoothed elevation profile is plotted above each cross-section and a profile of the recovered crustal thickness is overplotted. We use different color scales for crust and mantle shear wave speeds. To diminish the appearance of small lateral differences as vertical stripes, smoothing has been applied for plotting purposes by averaging velocity values at each depth with those of neighboring horizontal grid points in the crust and mantle. Crustal structure is smoothed by taking a weighted average that includes the four nearest grid points in map view. Mantle structure is similarly smoothed, but the weighted average includes the eight nearest grid points. Vertical smoothing is also used as described above in the discussion of Figure 11. The vertical exaggeration of the cross-sections is roughly 25:1 and the same horizontal scale is used for N-S and E-W cross-sections.

As with the depth-sections presented in Figure 11, the most pronounced shallow crustal velocity anomalies are from sedimentary basins, although vertical smoothing extends these features to greater depths. Profiles C-C' and F-F', for example, show that the Mississippi Embayment extends inland from the coast for hundreds of kilometers. The most pronounced velocity contrasts result from the location of the east-west velocity dichotomy in the crust and upper mantle, as will be discussed in more detail in Section 6.1 below. Slow mantle velocities exist from the Rocky Mountains to the west and are particularly low in the Basin and Range, which has been altered by extension. A discussion of the amplitude of observed mantle anomalies compared to previous work is presented in Section 6.2 below.

The relation between topography, crustal thickness, and crust and mantle velocities allow qualitative conclusions to be drawn regarding the support for high topography in the US. In general, surface topography within the US is not well correlated with crustal thickness. For example, the north-south profiles in Figure 11 reveal very little relation between the surface and Moho topography. Profile E-E', in particular, reveals crustal thickness to be anti-correlated with topography and substantial Moho topography exists under regions with almost no surface topography in Profiles F-F' and G-G'. In addition, the Basin and Range province is characterized by high elevations, but the crust is relatively thin. In all of these areas, however, high elevations with relatively thin crust are underlain by a slower and presumably less dense crust and mantle, indicative of a Pratt-type of compensation. There are exceptions, however. Running from west to east along Profile B-B', the highest elevations coincide with a mantle that is relatively slow and the crust is thick. Farther east in the Great Plains, the thinning crust and decreasing elevation are coincident suggesting an Airy-type of compensation.

The standard deviation (σ) of the ensemble of Monte-Carlo models computed at each grid point indicates the confidence level for velocity values through depth and across the study region. Average values for σ versus depth are shown in Figure 14a. Except near the surface, the average value of uncertainty is about 1.5% with this value increasingly slightly with depth. The RMS of velocities as a function of depth taken over the entire region of study is also shown in Figure 14 to be about 3%, except near the surface. Thus, lateral velocity anomalies are, on average, about twice the size of the uncertainties. The lower anomaly values observed in the middle crust are likely because topography is not allowed on the layer boundaries above and below to tradeoff with it, leading to a lower ensemble standard deviation. The jump in RMS anomaly values near 45 km depth is caused by the sampling of both crust and mantle velocities; the mean velocity value around 45 km depth is between typical crust and mantle velocities, therefore the typical deviations from this (in %) are greater. Figure 15 shows the amplitude and distribution of σ across the study region at the depths presented in Figure 11. At 4 km depth, σ is greatest near the edges of the study area, in part due to higher expected data errors caused by lower resolution. Low σ values at 10 km depth (Figure 15b) through much of the study region, as mentioned above, are due to the lack of boundaries above and below with which to trade-off. A parameterization that allows topography or more crustal layers would generate greater middle crustal σ values. In the lower crust (Figure 15c), σ is greater than in the mid-crust due to the tradeoff between wave speed and crustal thickness; similar values are observed in the upper mantle (Figure 15d) due to the same tradeoff. At 80 km (Figure

15e), σ is lower than at shallower depths and is more uniform. The uniformity extends to 120 km depth (Figure 15f), although the amplitude of σ increases slightly at this depth due to poorer sensitivity at greater depths as indicated in Figure 3.

Figure 14b shows the average standard deviation in the dispersion curves produced by the ensemble of acceptable models. Greater variability in model velocity values in the uppermost crustal layer results in the higher standard deviation values at short periods (i.e., < 15 s period). Rayleigh and Love wave phase speed variability is nearly constant at 0.5% while the Rayleigh wave group speed variability is higher due to the higher χ^2 misfit threshold used in the Monte-Carlo re-sampling.

6. Discussion

A detailed interpretation of the estimated 3D model is beyond the scope of this paper. We discuss three specific questions and emphasize using the model uncertainties to address them. First, we constrain the location of the east/west velocity dichotomy in the lower crust and uppermost mantle. Second, we compare the amplitude of the observed mantle velocity anomalies to those of the global model of *Shapiro and Ritzwoller* [2002]. Finally, we present alternative model parameterizations in the attempt to resolve the crustal Rayleigh/Love velocity discrepancy discussed in Section 4 above.

6.1. East-West Velocity Dichotomy

The difference in crustal and uppermost mantle shear wave speeds between faster tectonically stable eastern US and the slower tectonically active western US is visible in the horizontal and vertical cross-sections presented in Figures 11 and 13. This is also a feature of other tomographic models and distinguishes the tectonically younger features of the western US from the older structures farther east. Here, we use the ensemble of models from the Monte-Carlo procedure to estimate the location of and uncertainty in this velocity dichotomy.

Velocity values for the lower crust and at 80 km depth are sorted for the ensemble of 100 acceptable models at each grid point. The sorted values are compiled for all grid points to develop a set of sorted maps. Contours are plotted through the 20th and 80th maps (which can be thought of as the 20th and 80th percentile) at 3.75 km/s in the lower crust and at 4.55 km/s at 80 km depth. These results are shown in Figure 16. In the lower crust (Figure 16a), the western velocity contrast roughly follows the Rocky Mountain Front from Wyoming to the south. This contrast occurs quickly. In fact, examining the lower crustal velocity values across a variety of latitudes, it is clear that this contrast is abrupt, with a velocity change of roughly 300 km/s occurring over less than 100 km laterally. This abruptness is also captured by in the difference between the 20th and 80th percentile of the model where the difference in position between the fast and slow contour along the Rocky Mountain Front is small. In the eastern US, the 20th percentile contour outlines the southeastern edge between the shield and the Appalachian Highlands farther east. However, this 20th percentile velocity contour does not precisely follow the western edge of the Appalachian highlands as plotted in Figure 2, which is an indication of the lower resolution in the eastern US. Another interesting feature is an outline of the Mid-Continental Rift (MCR), oriented in a NNE-SSW direction in the central US. This feature is subtle in velocity depth- and cross-sections but clearly appears in these contours, with a location that agrees with the configuration determined through gravity observations.

At 80 km depth in the mantle, a similar set of contours outlines the eastern edge of the slower western US. However, the location of these contours now aligns with the Rocky Mountain Front in the northern part of the study area and lies farther east in southern portions. Creating the 20th and 80th percentile contours with slightly faster and slower velocity values gave similar results. The extent of the slower contour farther to the east provides an outline of the cratonic lithosphere. Overall, the range of locations is sufficiently narrow to constrain the dichotomy in the lower crust and uppermost mantle and to observe that these locations are not necessarily aligned. The fact that slower and presumably less dense mantle material often extends farther east than the Rocky Mountain Front suggests that mantle compensation plays a role in the high topography of that region. The cause of this difference could be erosion of mantle lithosphere of the craton due to volatiles.

6.2. Comparison with a Global Scale Model

A comparison with previous global tomography models identifies the effect of the improved resolution of this study. Resolution has been improved both vertically and laterally. Improved vertical resolution results from the fact that ambient noise EGFs permit much shorter period dispersion measurements. Improved lateral resolution results from the inter-station dispersion measurements being made over a shorter baseline that teleseismic observations. Figure 17b shows a cross section from the model of *Shapiro and Ritzwoller* [2002] compared to our results (Figure 17a) at 40°N (see location in Figure 13a). For reference, the difference between Figure 17a,b is plotted in Figure 17c. The primary differences are in the mantle, but some of the crustal differences highlight the better crustal resolution afforded by ambient noise tomography. For example, the slower velocities in the upper crust beneath the Basin in Range seen in Figure 17a and the correlation of these low velocities with high topography illustrates the higher resolution. More significantly, the amplitudes of the velocity anomalies in the global model are much larger than those revealed by ambient noise. Considering the full range of models in our Monte-Carlo ensemble we find that the lower range of values in the slow mantle anomaly between 245° and 250°E is roughly 4.1 km/s, which is lower than the 4.2 km/s reported in Figure 17b. However, the fast end of the model ensemble for mantle velocities between 255° and 265°E is roughly 4.65 km/s which is less than the 4.75 km/s observed in the same region by *Shapiro and Ritzwoller* [2002].

The model of *Shapiro and Ritzwoller* [2002] was created using diffraction tomography, with broad finite frequency sensitivity kernels. *Ritzwoller et al.* [2002] assessed differences in the results between ray theoretical and diffraction tomography. Finite frequency kernels systematically produce higher anomaly amplitudes. We attribute the unreconciled differences observed in Figure 17 to the effects of finite frequency tomography at teleseismic distances overestimating anomaly amplitudes. This provides evidence that the effective width of the sensitivity kernels for finite frequency tomography should be much narrower than the full sensitivity kernel, closer to ray theory. It also highlights the general problem of estimating amplitudes accurately using single-station teleseismic methods.

6.3. Resolving the Rayleigh Love Wave Speed Discrepancy

As presented in Section 4, relatively poor data fit was observed in western portions of the study area where resolution is best. High χ^2 values in this area due to underestimation of data error are unlikely. Furthermore, the wide-spread problem of under-predicting Love wave speeds while over-predicting Rayleigh wave speeds at short periods is consistent with radial anisotropy in the crust (i.e., $Vsh \neq Vsv$). Seismic anisotropy is caused by the organization of material and radial anisotropy is principally caused by aligned minerals in the crust and mantle. Mapping radial anisotropy in the upper mantle using fundamental mode Rayleigh and Love waves is a well established technique (e.g., *Tanimoto and Anderson* [1984], *Montagner* [1991]). *Shapiro et al.* [2004] used shorter period Rayleigh and Love wave observations to constrain radial anisotropy in the crust of Tibet. They attribute this phenomenon to the effect of aligned mica crystals due to crustal flow. However, widespread application of such analysis has been limited by a lack of short period dispersion observations. Considering the tectonic history of the western US and specifically the Cenozoic extension that may have caused similar material organization, radial anisotropy is a reasonable parameterization to satisfy the widespread crustal Rayleigh/Love discrepancy we observe as it has been documented before. Furthermore, the data fit compared to isotropic models improves significantly by allowing radial anisotropy in the crust. A parameterization permitting low velocity zones (LVZ) in the crust also improves data fit to a lesser degree but LVZs have been documented only in smaller regions and are not thought to be ubiquitous features. Still, it is another parameterization we consider here.

Our method of quantifying radial anisotropy is somewhat *ad hoc* but obtains more than sufficient precision when compared to forward modeling tests. We prefer this method for its speed and due the the limited bandwidth of Love wave measurements (i.e., 8 - 20 s period), which is insufficient to solve for a *Vsh* model directly. Our method starts with all acceptable 1D isotropic velocity models in the Monte-Carlo model ensemble at each grid point. A grid search over small perturbations (-500 m/s to 500 m/s) in the velocity of either the middle or lower crustal layer is performed while leaving the rest of the model intact. We calculate dispersion curves for each perturbation in the grid search, and χ^2

misfit values for Rayleigh and Love wave phase speed curves are computed. The model with the best Rayleigh wave χ^2 misfit is chosen as the *Vsv* model while the best Love wave phase speed model is chosen for *Vsh*. Whichever of the upper or lower crustal model suites shows greatest improvement in data fit is preferred. We report the least anisotropic model from that ensemble, which in many cases is an isotropic model, and present an interpretation below.

To ensure the reliability of the *ad hoc* method we employ, we first perform tests using the anisotropic 'MINEOS' code of *Masters et al.* [2007]. We create synthetic dispersion curves for models possessing radial anisotropy in the crust. We then attempt to recover these models using the procedure outlined above in the period range of our dispersion measurements. We find that the *ad hoc* procedure recovers the initial model within 5 m/s, which is satisfactory in light of the 200 m/s signals often observed.

An example of the data fit with and without anisotropy at a point in northwest Utah is shown in Figure 18 (the location is labeled as a grey star in Figure 1). This example is typical of our results where at short periods the isotropic model predicted too great a velocity for Rayleigh wave observations and too low a value for Love waves. We achieve improved data fit by allowing the *Vsh* and *Vsv* in the middle crust to vary as seen by the blue dispersion curves in Figure 18a.

When, instead, we remove the requirement of monotonically increasing crustal velocity and increase the number of crustal layers to 4, similar improvement in data fit is observed and are shown in green in Figure 18a with the related model in Figure 18b. Still, the recovered data fit is not as good as that derived from the radial anisotropic parameterization.

As a broader test of which parameterization is preferable, we attempt to fit the data using a LVZ parameterization in an area of Nevada where radial anisotropy improves data fit and where crustal LVZs have been documented. *Ozalaybey et al.* [1997] found thin crustal LVZs (~5 km thick) at points in this area using a joint receiver function/surface wave technique. For the 93 grid points tested, this procedure was not able to obtain the quality of fit observed using the radial anisotropy technique discussed above as shown by the results in Table 1. It is possible that crustal LVZs could provide better data fit than what we observe but based on the work of *Ozalaybey et al.* [1997], we anticipate that a much greater number of crustal layers would be needed as well as other constraints on structure and velocity of the area.

Finally, looking at the spatial distribution of points suggesting radial anisotropy in the crust provides more information about the region. Although we test for radial anisotropy in the middle or lower crust and could assign independent *Vsh* and *Vsv* values through the 3D velocity model, we prefer to present just the spatial distribution and strength of observed crustal radial anisotropy. Figure 19 shows observed radial anisotropy in the crust from the best fitting and most isotropic models of the ensemble of models at each geographical grid point. In Figure 19a we see that positive anisotropy (as [*Vsv/Vsh* - 1]*100) is more prevalent. A broad continuous regions of radial anisotropy exists in the Basin and Range. Other smaller features are sometimes more difficult to interpret. Looking instead at the least anisotropic model (Figure 19b), only features that are more robust remain. We see correlation of signals with two main types of known features: sedimentary basins and extensional regions. The Anadarko, Appalachian, and Green River basins are clearly outlined. In these cases, the layering of sediments may cause different *Vsh* and *Vsv* values in the upper crust and some improvement in data fit is observed from allowing radial anisotropy in the middle crust. Other causes for apparent anisotropy have been shown, however, such as the effect of a lateral contrast across which Love and Rayleigh waves sample differently (e.g., *Levshin and Ratnikova* [1984]). The radial anisotropy signal around basins may be of this nature. Radial anisotropy on the order of 2 - 4 % is observed through much of the Basin and Range, extending southeast to the Rio Grande Rift. The removal of mantle lithosphere and related mantle flow could have some effect but the strength of the Rayleigh/Love wave speed discrepancy at short periods indicates the the influence is from shallower sources. A more likely explanation would be that the observed radial anisotropy is due to organization of crustal materials effected during Cenozoic extension. *Shapiro et al.* [2004] attributed observed radial anisotropy to the alignment of mica crystals in the crust. The effects of other compositional organization, such as aligned cracks (e.g., *Crampin and Peacock* [2005]), or layers (e.g., *Crampin* [1970]) have also been shown to cause seismic anisotropy. The multiplicity of sources of radial anisotropy must be considered when interpreting these results. Presentation of 3D distribution of *Vsh* and *Vsv* and further investigation of alternative parameterizations awaits more exhaustive studies of the using data from the USArray/Transportable Array.

7. Conclusions

We created a high resolution shear velocity model of the crust and uppermost mantle through much of the continental United States as determined by surface wave ambient noise tomography (ANT). Using broad-band, continental-scale Rayleigh and Love wave ANT results developed by *Bensen et al.* [2007b], we employ a two-step procedure to obtain

3D shear wave speed from the surface down to roughly 150 km depth. First, a linearized inversion is performed to find the best fitting model at each grid point on a 0.5° x 0.5° grid. Second, a Monte-Carlo procedure is carried out to estimate the amplitude and distribution of model uncertainty. Inferences of structure are made from the model including: an observation of the abruptness of velocity transitions that mark boundaries between tectonic provinces, varying degrees of homogeneity in crustal velocities, distinct instances of Airy and Pratt elevation compensation, a clearer outline of the North American Craton, and more. Recovered crustal thickness is similar to the model Crust 2.0 of *Bassin et al.* [2000]. Additionally, we observe a discrepancy between the observed Rayleigh and Love wave speeds as predicted by an isotropic model. Allowing radial anisotropy or low velocity zones in the crust and often improves the data fit. It is likely that radial anisotropy exists in the crust through extensional provinces where values of $Vsh/Vsv > 1$ in are commonly observed. A more exhaustive study of alternative model parameterization incorporating other data (e.g., receiver functions) would help resolve this ambiguity. This model will be helpful in future qualitative and quantitative work in the area. Natural extensions of this work include the incorporation of earthquake based measurements for both increased path density and augmented bandwidth.

8. Acknowledgements

All of the data used in this research were downloaded either from the IRIS Data Management Center or the Canadian National Data Center (CNDC). This research was supported by a contract from the US Department of Energy, DE-FC52-2005NA26607, and two grants from the US National Science Foundation, EAR-0450082. We are grateful for the support of Chuck Meertens through this project and the GEON project support for Bensen (EAR-0408228).

References

().

Alsina, D., R. L. Woodward, and R. K. Snieder (1996), Shear wave velocity structure in North America from large-scale waveform inversions of surface waves, *J. Geophys. Res.*, *101*(B7), 15,969–15,986.

Barmin, M. P., M. H. Ritzwoller, and A. L. Levshin (2001), A fast and reliable method for surface wave tomography, *Pure Appl. Geophys.*, *158*(8), 1351–1375.

Bassin, C., G. Laske, and G. Masters (2000), The current limits of resolution for surface wave tomography in North America, *EOS Trans. AGU*, *81*, F897.

Bensen, G. D., M. H. Ritzwoller, M. P. Barmin, A. L. Levshin, F. Lin, M. P. Moschetti, N. M. Shapiro, and Y. Yang (2007a), Processing seismic ambient noise data to obtain reliable broad-band surface wave dispersion measurements, *Geophys. J. Int.*, *169*, 1239–1260.

Bensen, G. D., M. H. Ritzwoller, and N. M. Shapiro (2007b), Broad-band ambient noise surface wave tomography across the united states, *J. Geophys. Res.*, "accepted".

Blackwell, D., J. Steele, and L. Carter (1990), Heat flow patterns of the North American continent: A discussion of the DNAG Geothermal Map of North America.

Christensen, N. I., and W. D. Mooney (1995), Seismic velocity structure and composition of the continental crust: A global view, *J. Geophys. Res.*, *100*(B6), 9761–9788.

Chulick, G. S., and W. D. Mooney (2002), Seismic structure of the crust and uppermost mantle of North America and adjacent oceanic basins: A synthesis, *Bull. Seis. Soc. Am.*, *92*(6), 2478–2492.

Crampin, S. (1970), The dispersion of surface waves in multilayered anisotropic media, *Geophys. J. Astr. Soc.*, *21*, 387–402.

Crampin, S., and S. Peacock (2005), A review of shear-wave splitting in the compliant crack-critical anisotropic Earth, *Wave Motion*, *41*(1), 59–77.

Crotwell, H. P., and T. J. Owens (2005), Automated receiver function processing, *Seis. Res. Lett.*, *76*(6), 702–709.

Dziewonski, A. M., and D. L. Anderson (1981), Preliminary reference Earth model, *Phys. Earth Plan. Int.*, *25*(4), 297–356.

Ekström, G., J. Tromp, and E. W. F. Larson (1997), Measurements and global models of surface wave propagation, *J. Geophys. Res.*, *102*(B4), 8137–8157.

Forsyth, D. W., and A. Li (2005), Array-analysis of Two-dimensional Variations in Surface Wave Phase Velocity and Azimuthal Anisotropy in the Presence of Multipathing Interference, *Seismic Earth: Array Analysis of Broadband Seismograms*, pp. 81–98.

Gao, W., S. P. Grand, W. S. Baldridge, D. Wilson, M. West, J. F. Ni, and R. Aster (2004), Upper mantle convection beneath the central Rio Grande Rift imaged by P and S wave tomography, *J. Geophys. Res.*, *109*(B03), 3305–3305.

Godey, S., R. K. Snieder, A. Villaseñor, and H. M. Benz (2003), Surface wave tomography of North America and the Caribbean using global and regional broad-band networks: phase velocity maps and limitations of ray theory, *Geophys. J. Int.*, *152*(3), 620–632.

Grand, S. P. (1994), Mantle shear structure beneath the Americas and surrounding oceans, *J. Geophys. Res.*, *99*(B6), 11,591–11,622.

Grand, S. P. (2002), Mantle shear-wave tomography and the fate of subducted slabs, *Philosophical Transactions: Mathematical, Physical and Engineering Sciences*, *360*(1800), 2475–2491.

Herrmann, R. B. (1987), Computer programs in seismology, *St. Louis University, St. Louis, Missouri.*

Jones, C. H., H. Kanamori, and S. W. . Roecker (1994), Missing roots and mantle "drips": Regional Pn and teleseismic arrival times in the southern Sierra Nevada and vicinity, California, *J. Geophys. Res.*, *99*(B3), 4567–4601.

Karlstrom, K. E., et al. (2002), CD-ROM working group. 2002. Structure and evolution of the lithosphere beneath the Rocky Mountains: initial results from the CD-ROM experiment, *GSA Today*, *12*(3), 4–10.

Keilis-Borok, V. I., and T. B. Yanovskaya (1967), Inverse problems in seismology (structural review), *Geophys. J. Astr. Soc.*, *13*, 223–234.

Kennett, B. L. N., E. R. Engdahl, and R. Buland (1995), Constraints on seismic velocities in the Earth from traveltimes, *Geophys. J. Int*, *122*(1), 108–124.

Laske, G., and G. Masters (1997), A global digital map of sediment thickness, *EOS Trans. AGU*, *78*, 483.

Lee, W. B., and S. C. Solomon (1978), Simultaneous inversion of surface wave phase velocity and attenuation: Love waves in western North America, *J. Geophys. Res.*, *83*(B7), 3389–3400.

Levshin, A., and L. Ratnikova (1984), Apparent anisotropy in inhomogeneous media, *J. Astron. Soc.*, *76*(1), 65–69.

Levshin, A. L., V. F. Pisarenko, and G. A. Pogrebinsky (1972), On a frequency-time analysis of oscillations, *Ann. Geophys.*, *28*(2), 211–218.

Li, A., D. W. Forsyth, and K. M. Fischer (2003), Shear velocity structure and azimuthal anisotropy beneath eastern North America from Rayleigh wave inversion, *J. Geophys. Res.*, *108*(10.1029).

Lin, F., M. P. Moschetti, and M. H. Ritzwoller (2007), Surface wave tomography of the western United States from ambient seismic noise: Rayleigh and Love wave phase velocity maps, *Geophys. J. Int.*, submitted.

Marone, F., and B. Romanowicz (2007), Non-linear crustal corrections in high-resolution regional waveform seismic tomography, *Geophys. J. Int.*, *170*(1), 460–467.

Marone, F., Y. Gung, and B. Romanowicz (2007), Three-dimensional radial anisotropic structure of the North American upper mantle from inversion of surface waveform data, *Geophys. J. Int.*, *171*(1), 206–222, doi:10.1111/j.1365-246X.2007.03465.x.

Masters, G., M. P. Barmine, and S. Kientz (2007), MINEOS user manual, *California Institute of Technology*.

Montagner, J. P. (1991), Global upper mantle tomography of seismic velocities and anisotropies, *J. Geophys. Res.*, *96*(B12), 20,337–20,351.

Moschetti, M. P., M. H. Ritzwoller, and N. M. Shapiro (2007), Surface wave tomography of the western United States from ambient seismic noise: Rayleigh wave group velocity maps, *Geochem. Geophys. Geosys.*, *8*(Q08010), doi:10.1029/2007GC001655.

Mosegaard, K., and A. Tarantola (1995), Monte Carlo sampling of solutions to inverse problems, *J. Geophys. Res.*, *100*(B7), 12,431–12,448.

Nolet, G. (1990), Partitioned waveform inversion and two-dimensional structure under the network of autonomously recording seismographs, *J. Geophys. Res.*, *95*(B6), 8499–8512.

Ozalaybey, S., M. K. Savage, A. F. Sheehan, J. N. Louie, and J. N. Brune (1997), Shear-wave velocity structure in the northern Basin and Range province from the combined analysis of receiver functions and surface waves, *Bull. Seis. Soc. Am.*, *87*(1), 183–199.

Ramachandran, K., S. E. Dosso, G. D. Spence, R. D. Hyndman, and T. M. Brocher (2005), Forearc structure beneath southwestern British Columbia: A three-dimensional tomographic velocity model, *J. Geophys. Res.*, *110*(B2), 2303(17), doi: 10.1029/2004JB003258.

Ritzwoller, M. H., and A. L. Levshin (1998), Eurasian surface wave tomography - group velocities, *J. Geophys. Res.*, *103*(B3), 4839–4878.

Ritzwoller, M. H., N. M. Shapiro, M. P. Barmin, and A. L. Levshin (2002), Global surface wave diffraction tomography, *J. Geophys. Res.*, *107*(B12), 2335–2347, doi: 10.1029/2002JB001777.

Sambridge, M., and K. Mosegaard (2002), Monte Carlo methods in geophysical inverse problems, *Rev. Geophys*, *40*(3), 3–32.

Shapiro, N. M., and M. H. Ritzwoller (2002), Monte-Carlo inversion for a global shear-velocity model of the crust and upper mantle, *Geophys. J. Int.*, *151*(1), 88–105.

Shapiro, N. M., M. H. Ritzwoller, P. H. Molnar, and V. Levin (2004), Thinning and flow of Tibetan crust constrained by seismic anisotropy, *Science*, *305*(5681), 233–236.

Snelson, C. M., T. J. Henstock, G. R. Keller, K. C. Miller, and A. Levander (1998), Crustal and uppermost mantle structure along the Deep Probe seismic profile, *Rocky Mountain Geology*, *33*(2), 181–198.

Snieder, R. K. (1988), Large-scale waveform inversions of surface waves for lateral heterogeneity 1. Theory and numerical examples, *J. Geophys. Res.*, *93*(B10), 12,055–12,065.

Tanimoto, T., and D. L. Anderson (1984), Mapping convection in the mantle, *Geophys. Res. Lett.*, *11*(4), 287–290.

Tarantola, A., and B. Valette (1982), Generalized nonlinear inverse problems solved using the least squares criterion, *Rev. Geophys. Space Phys*, *20*(2), 219–232.

Thurber, C., H. Zhang, F. Waldhauser, J. Hardebeck, A. Michael, and D. Eberhart-Phillips (2006), Three-dimensional compressional wavespeed model, earthquake relocations, and focal mechanisms for the Parkfield, California, region, *Bull. Seis. Soc. of Am.*, *96*(4 B), 38–49.

Trampert, J., and J. H. Woodhouse (1996), High resolution global phase velocity distributions, *Geophys. Res. Lett.*, *23*(1), 21–24.

van der Lee, S. (2002), High-resolution estimates of lithospheric thickness from Missouri to Massachusetts, USA, *Earth Plan. Sci. Lett.*, *203*(1), 15–23.

van der Lee, S., and A. Frederiksen (2005), Surface wave tomography applied to the North American upper mantle, *Geophysical monograph*, *157*, 67–80.

van der Lee, S., and G. Nolet (1997), Upper mantle S velocity structure of North America, *J. Geophys. Res.*, *102*(B10), 22,815–22,838.

Villaseñor, A., M. H. Ritzwoller, A. L. Levshin, M. P. Barmin, E. R. Engdahl, W. Spakman, and J. Trampert (2001), Shear velocity structure of central Eurasia from inversion of surface wave velocities, *Phys. Earth Planet. Inter*, *123*(1), 169–184.

Weeraratne, D. S., D. W. Forsyth, K. M. Fischer, and A. A. Nyblade (2003), Evidence for an upper mantle plume beneath the Tanzanian craton from Rayleigh wave tomography, *J. Geophys. Res.*, *108*(B9), 2427–2446.

Wernicke, B. P., G. J. Axen, and J. K. Snow (1988), Basin and Range extensional tectonics at the latitude of Las Vegas, Nevada, *Bull. Geol. Soc. Am.*, *100*(11), 1738–1757.

Wilson, C. K., C. H. Jones, and H. J. Gilbert (2003), Single-chamber silicic magma system inferred from shear wave discontinuities of the crust and uppermost mantle, coso geothermal area, california, *J. Geophys. Res*, *108*, 1–16.

Yang, Y., M. H. Ritzwoller, A. L. Levshin, and N. M. Shapiro (2007), Ambient noise Rayleigh wave tomography across Europe, *Geophys. J. Int.*, *168*(1), 259–274.

Yao, H., R. D. van der Hilst, and M. V. de Hoop (2006), Surface-wave array tomography in SE Tibet from ambient seismic noise and two-station analysis-I. Phase velocity maps, *Geophys. J. Int.*, *166*(2), 732–744.

Yuan, H., and K. Dueker (2005), Upper mantle tomographic Vp and Vs images of the Rocky Mmountains in Wyoming, Colorado and New Mexico: Evidence for a thick heterogeneous chemical lithosphere, *Geophysical Monograph*, *154*, 329–345.

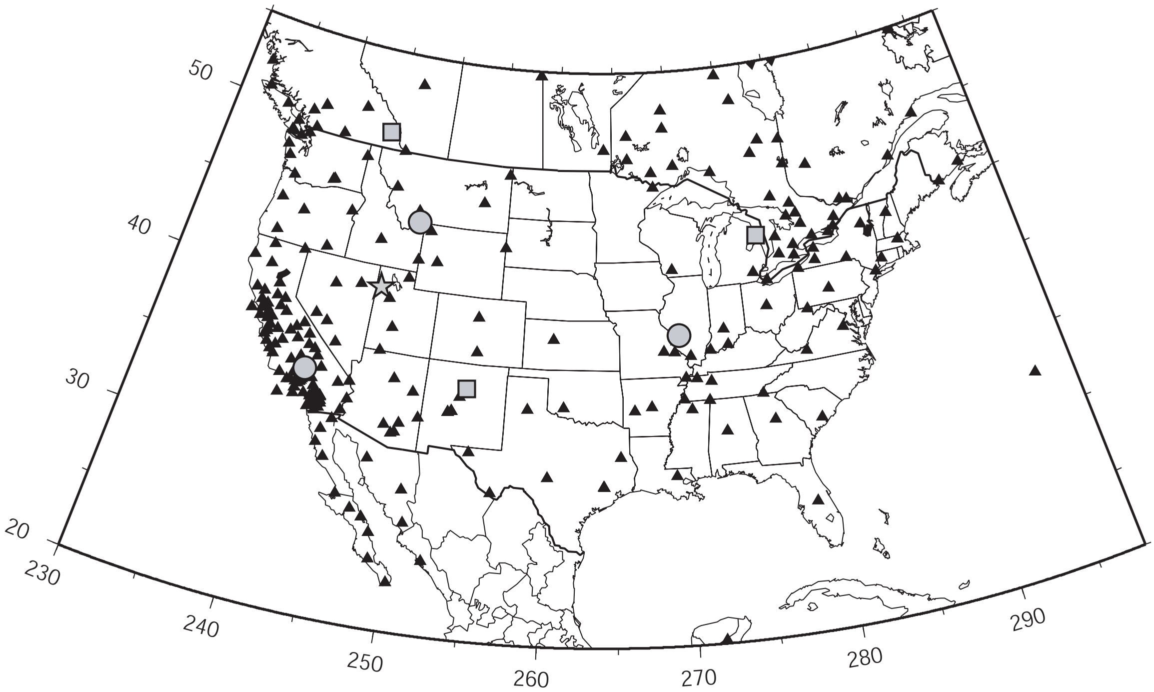

Figure 1. Map of the study area. Stations used for the experiment are shown as black triangles. Grey circles, squares and a star show the locations of data used for examples in Figures 7, 8 and 18, respectively.

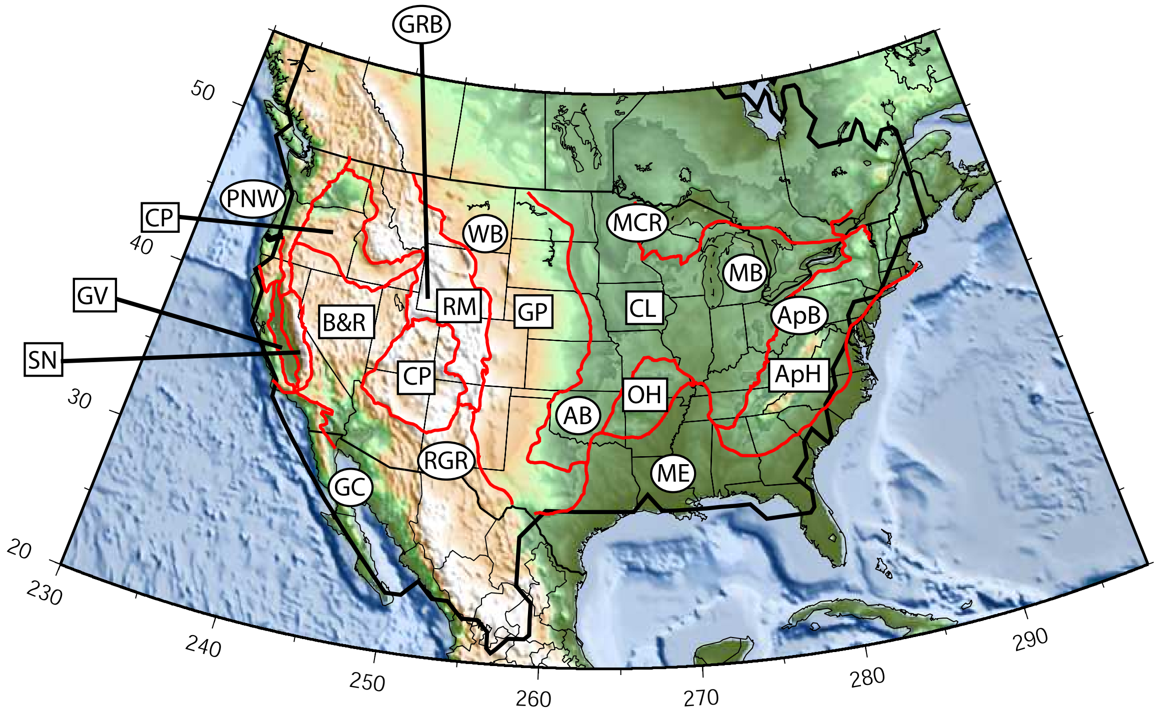

Figure 2. Regions and geographic features. The black contour envelops the area with lateral resolution better than 500 km for 16 s Rayleigh wave phase velocity tomography. Tectonic provinces are outlined in red and are labeled (bounded by rectangles) for reference. Features labeled above (from east to west) are as follows: Appalachian Highlands(ApH), Ouachita-Ozark Highlands (OH), Central Lowlands (CL), Great Plains (GP), Rocky Mountain Region (RM), Colorado Plateau (CP), Basin and Range (B&R), Columbia Plateau (CP), Sierra Nevada Mountains (SN), and Great Valley (GV). Other features are labeled (bounded by ellipses) as follows: Appalachian Basin (ApB), Michigan Basin (MB), Mississippi Embayment (ME), Mid-continental Rift (MCR), Anadarko Basin (AB), Williston Basin (WB), Rio Grande Rift (RGR), Green River Basin (GRB), Gulf of California (GC), and Pacific Northwest (PNW).

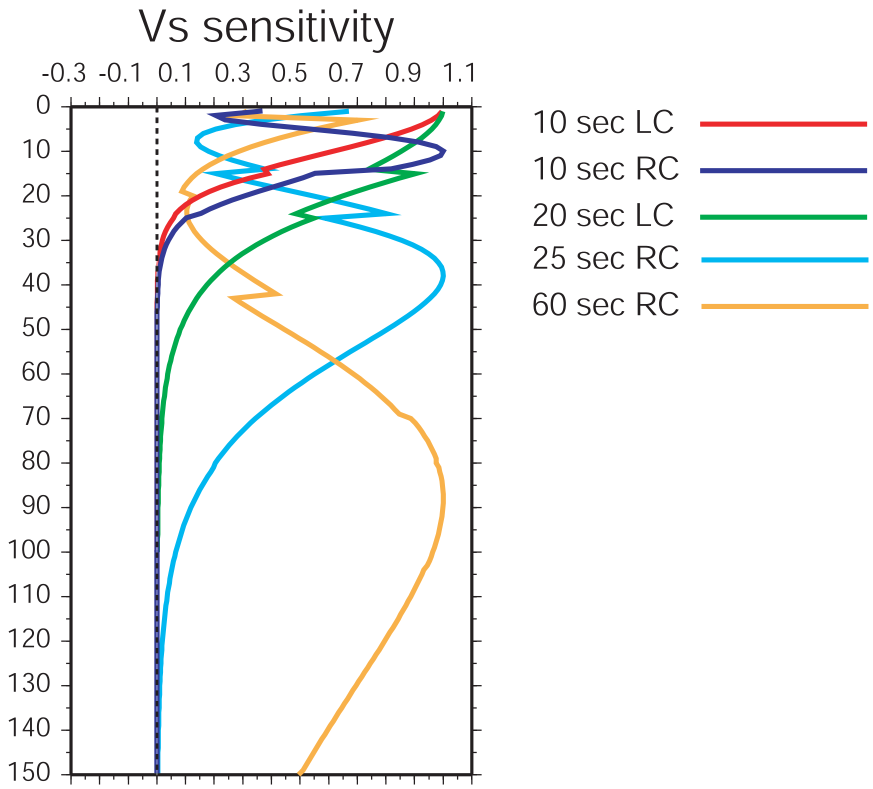

Figure 3. Sensitivity kernels for Rayleigh (labeled RC) and Love (labeled LC) wave phase speeds at a selection of periods.

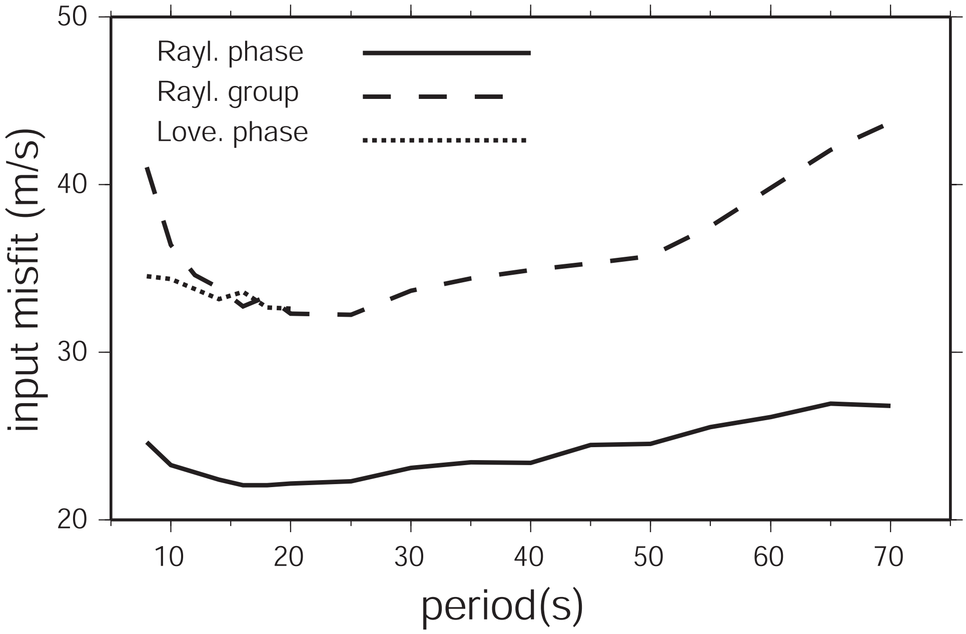

Figure 4. Average measurement uncertainty for Rayleigh wave group and phase and Love wave phase speed maps. These are the average values within which we attempt to fit the data.

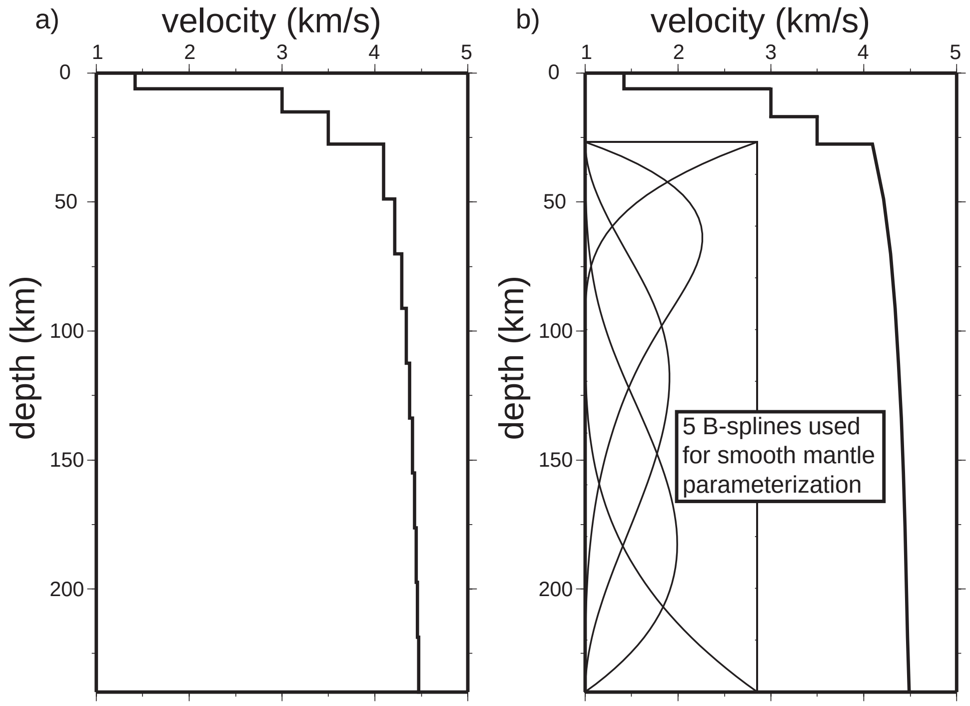

Figure 5. An illustration of the parameterization of the models used to create dispersion curves for the linearized inversion (a) and Monte-Carlo sampling (b). Initial thicknesses for the sediment layer and the crust are taken from *Laske and Masters* [1997] and *Bassin et al.* [2000] respectively. Fifteen layers are used in the mantle for the linearized inversion while five B-splines are used in the mantle for the Monte-Carlo re-sampling.

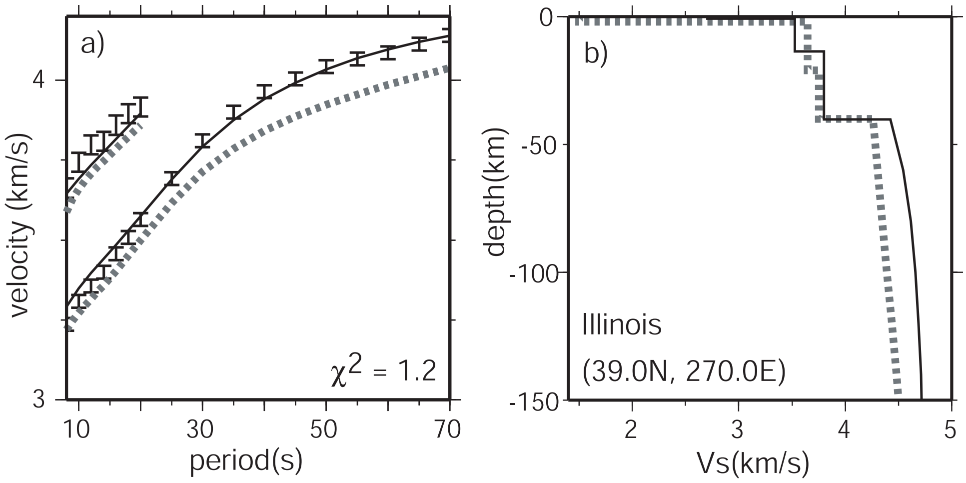

Figure 6. Examples of best fitting models and dispersion curves from the linearized inversion for a point in Illinois. The dispersion measurements and uncertainties are represented with error bars in (a). The input model in (b) and related dispersion curves in (a) are shown as grey dashed lines. The recovered models and dispersion curves are thin black lines in (b) and (a). The latitude, longitude and approximate location is listed in (b) and labeled as a grey circle in Figure 2. The model is a stack of constant velocity layers but for smooth mantle representation, we plot velocity values at the center of each mantle layer.

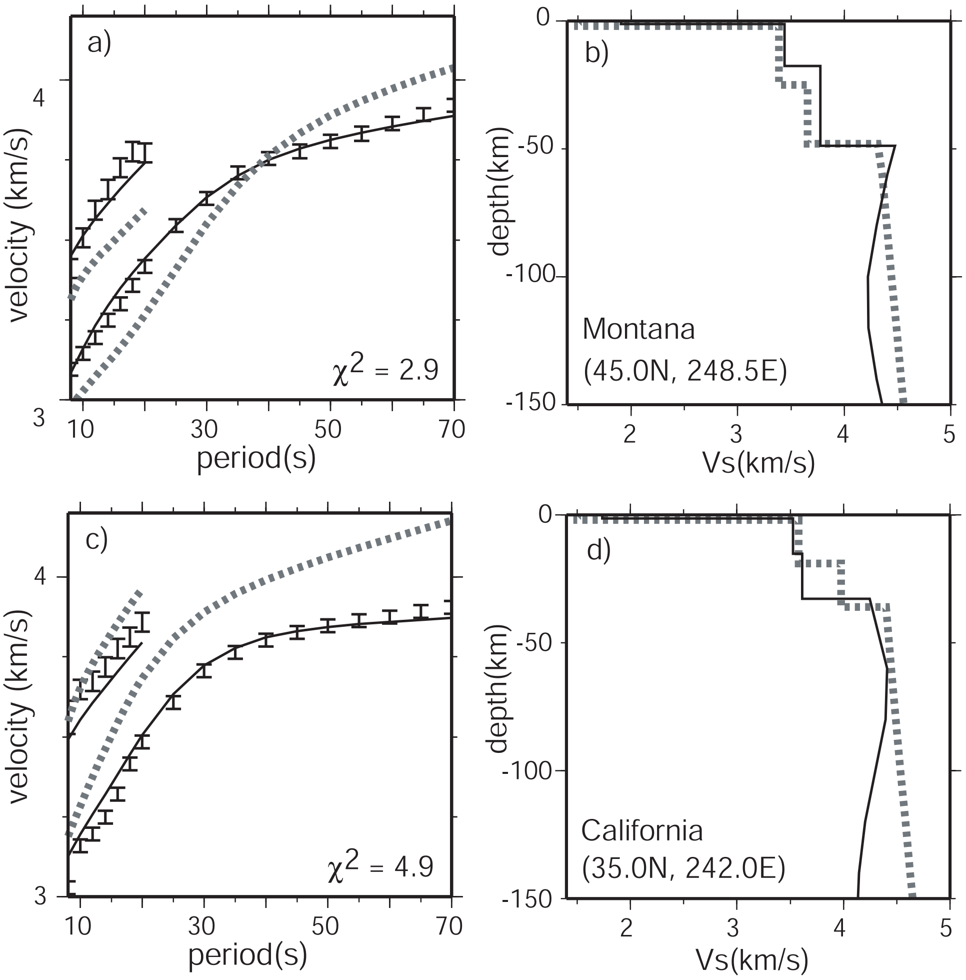

Figure 7. Same as Figure 7 but for points in California and Montana. χ^2 values are indicated in (a) and (c) and are toward the larger end of values seen in our study.

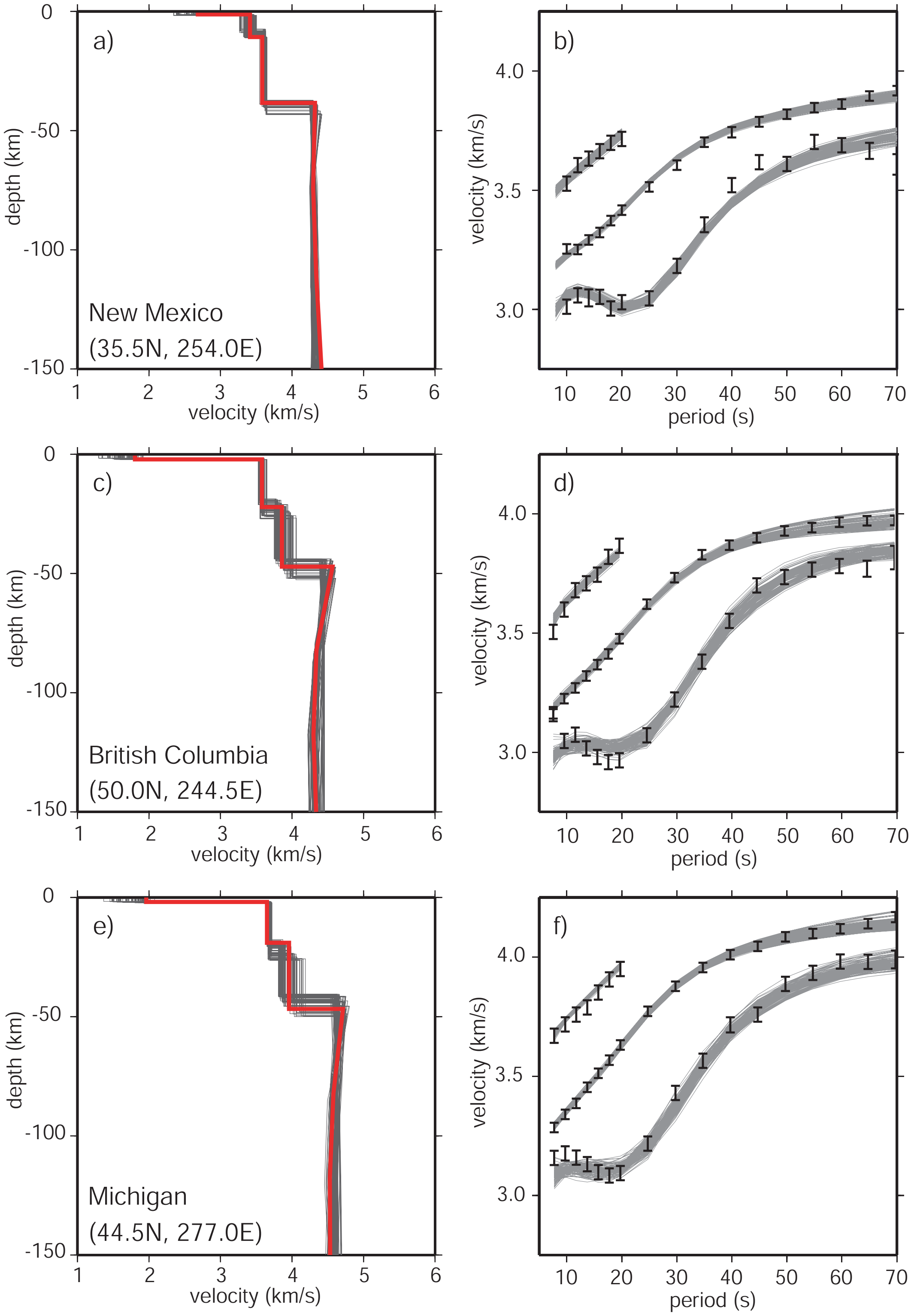

Figure 8. Examples of the input and output dispersion curves (error bars and grey lines, respectively, in (b), (d), and (f)), the resulting ensemble of Monte-Carlo models ((a), (c), and (e)). The "favored model" is highlighted in red. Locations of the examples presented here are shown as grey squares in Figure 2 and can be located with the latitude and longitude values in (a), (c) and (e).

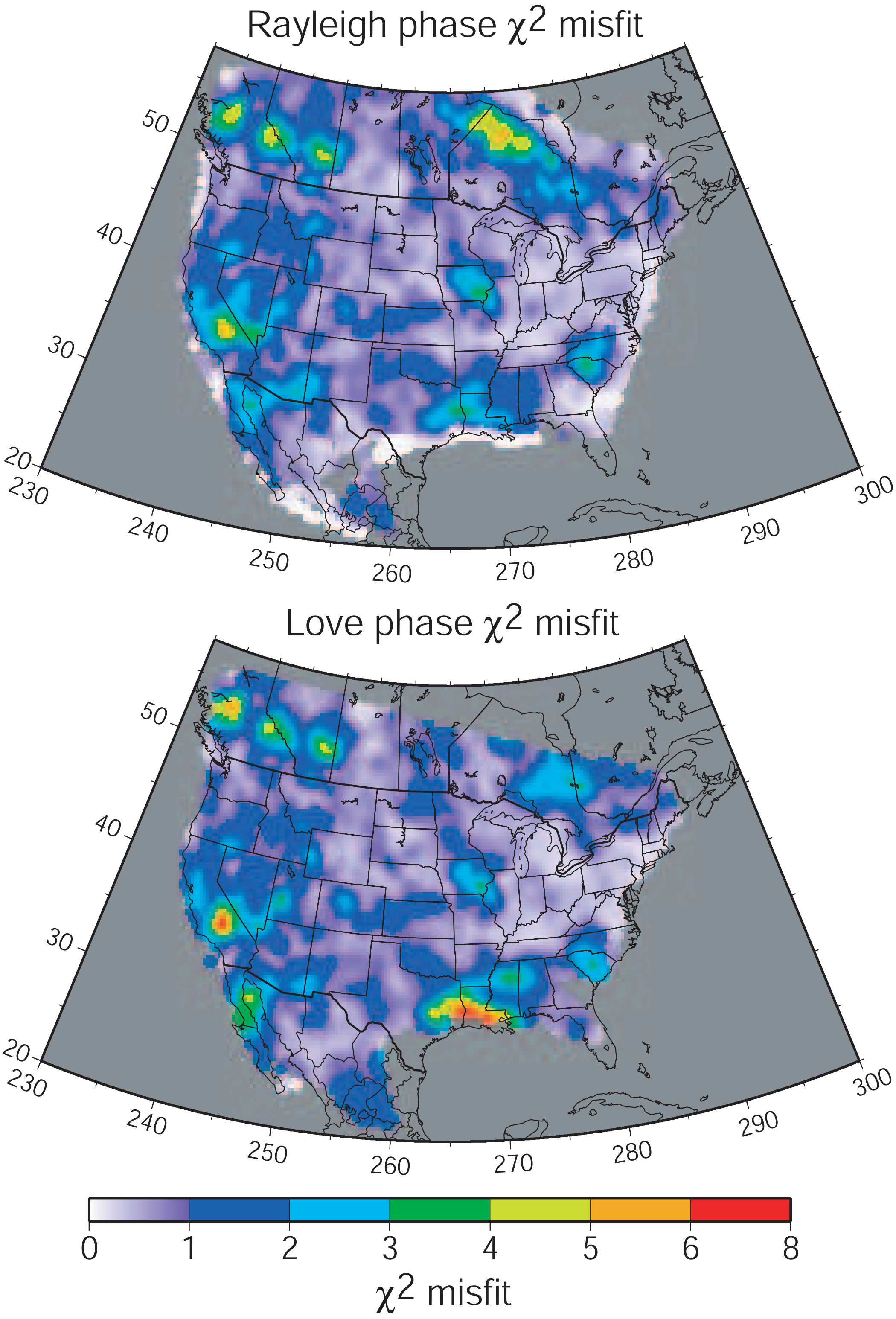

Figure 9. Rayleigh and Love wave phase velocity χ^2 misfit values for the best fitting models at each point as determined through linearized inversion. The χ^2 values listed in Figures 7a,c reflect the quality of fit shown here.

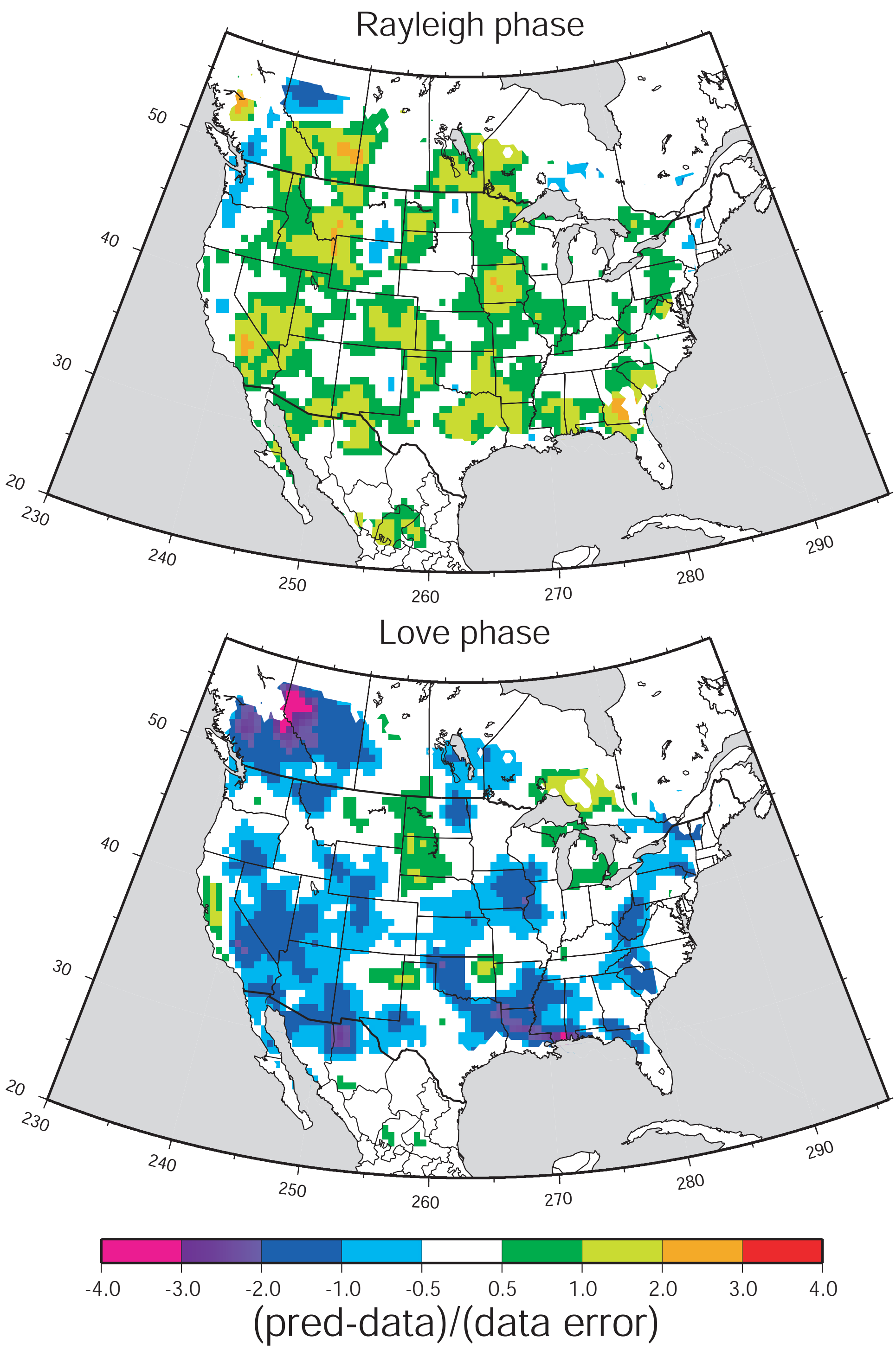

Figure 10. A representation of the short-period discrepancy between Rayleigh and Love waves from the "favored models." The difference of the model predicted and measured wave speed is divided by the data error at each point for each period. The results presented here are the average of values from 8 - 20 s period.

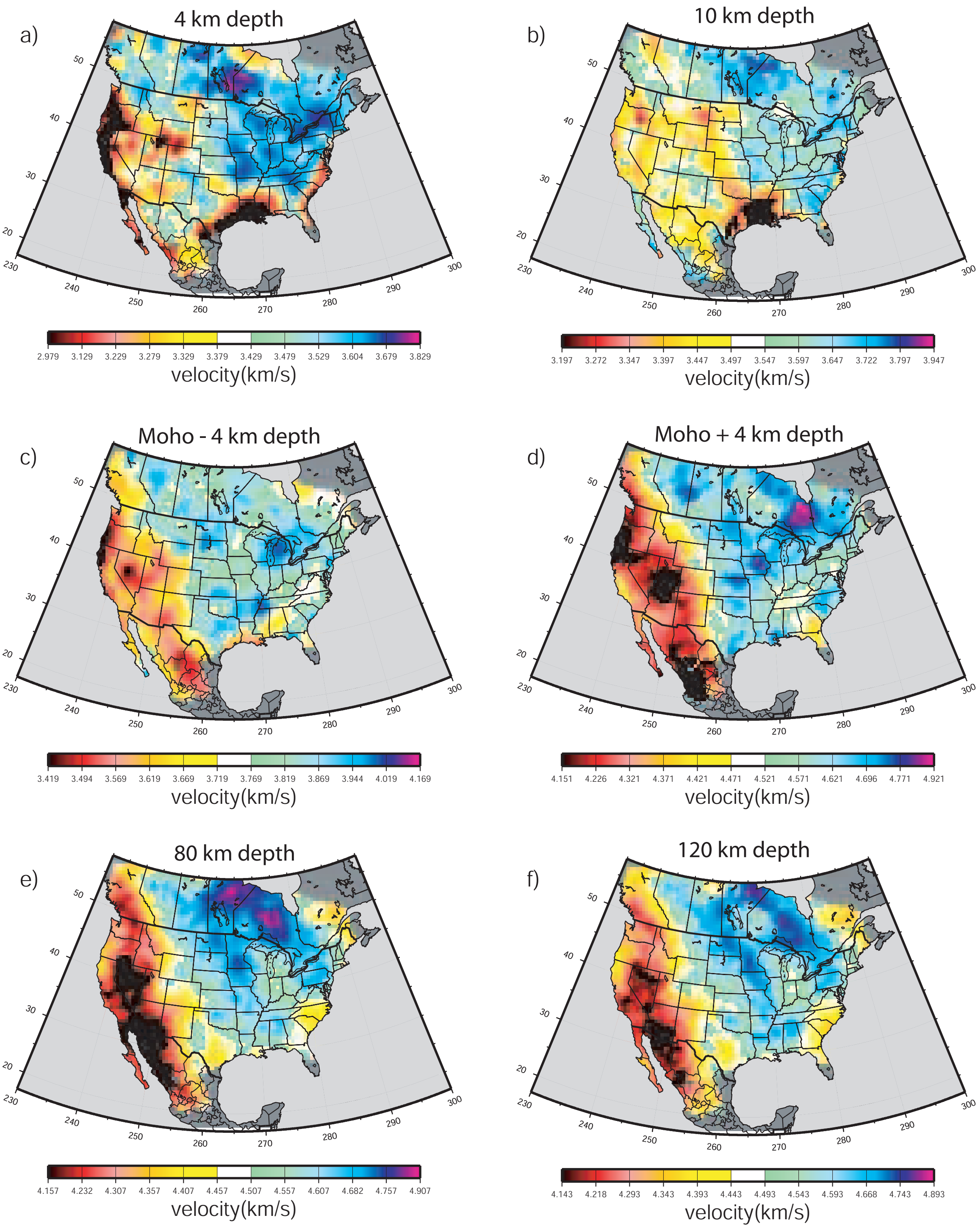

Figure 11. A selection of depth sections through the "favored model" after Monte-Carlo re-sampling. Vertical smoothing is applied in the crust and mantle as described in the text. Panels (c) and (d) show the velocity results at 4 km above and below the recovered Moho respectively.

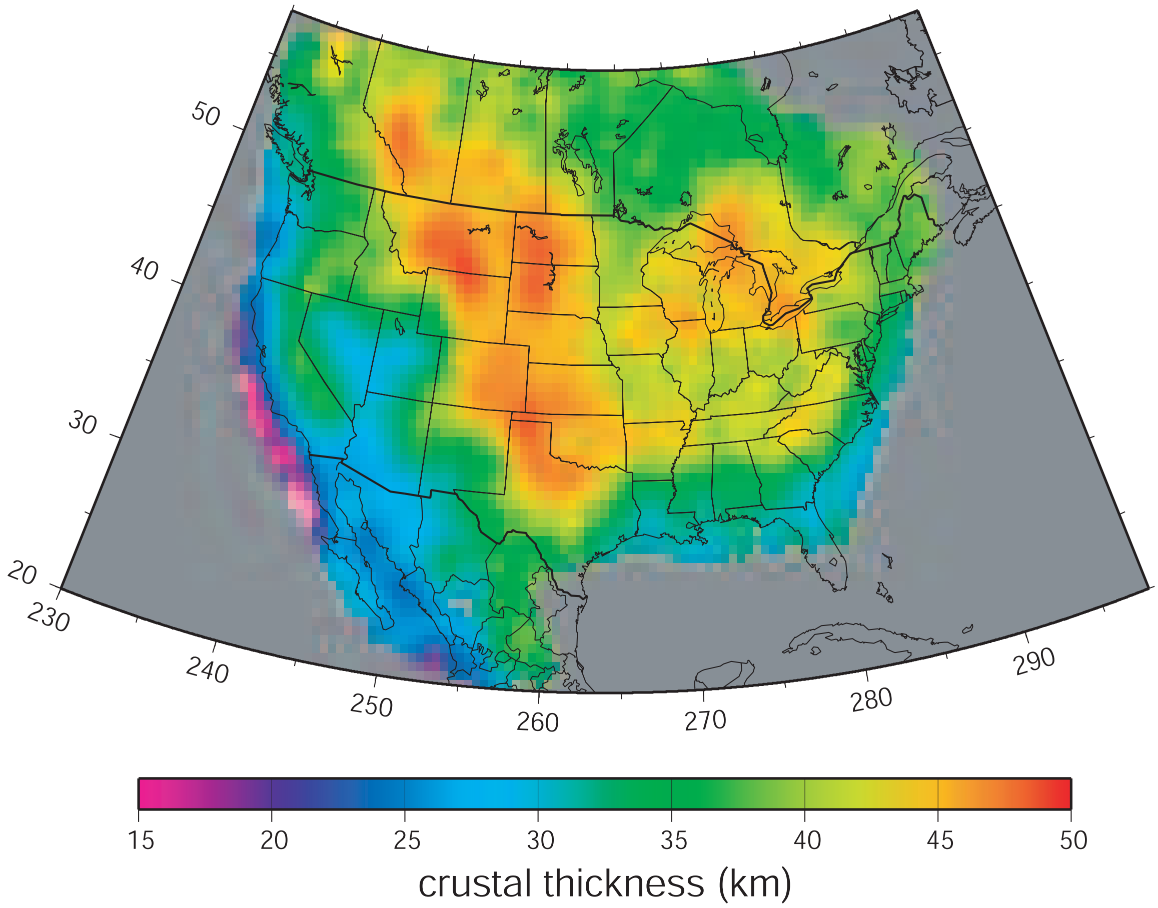

Figure 12. The crustal thickness recovered after the Monte-Carlo re-sampling. Crustal thickness is required to be within 5 km of the values of *Bassin et al.* [2000].

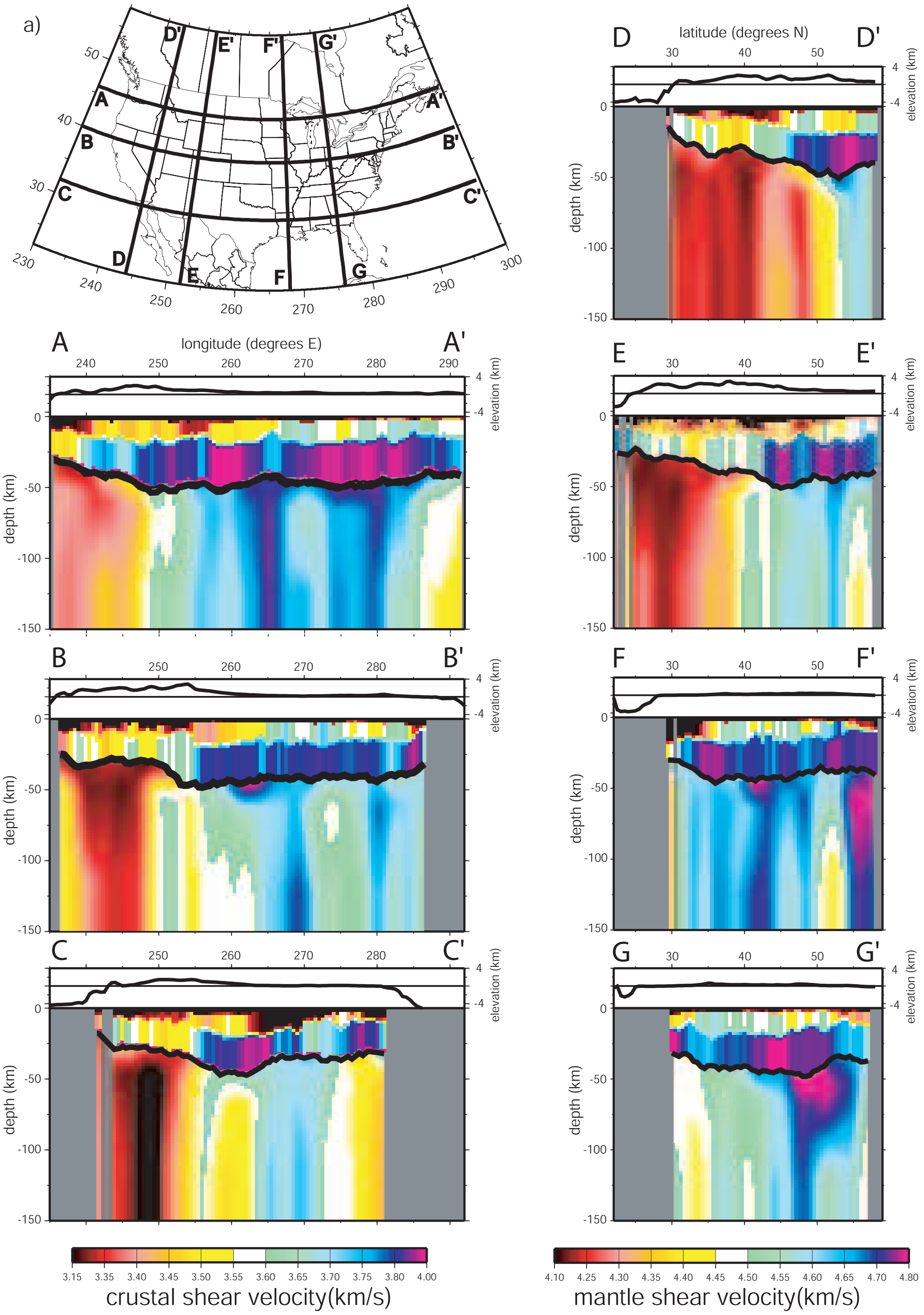

Figure 13. A selection of cross sections through the "favored models" after Monte-Carlo re-sampling. The locations of the cross-sections are indicated in (a) and the horizontal scales of all the cross-sections is the same. The recovered Moho is plotted in all cross-sections as a black line. Different color scales are used in the crust and mantle, as shown at the bottom of the figure.

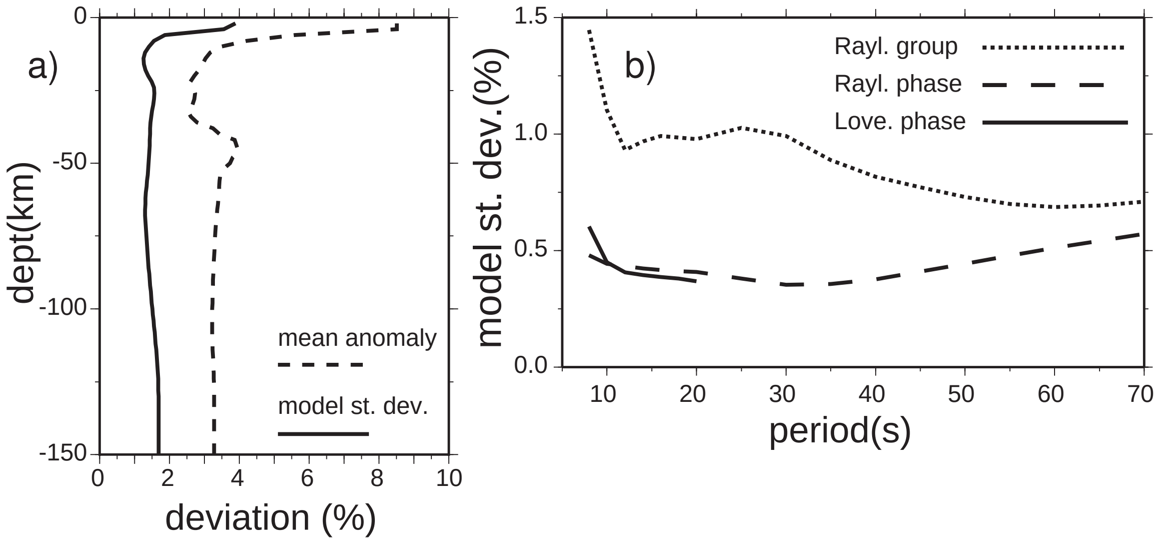

Figure 14. The average standard deviation of the resulting models is plotted vs. depth (a) and period (b). The mean of the absolute value of the velocity anomaly at each depth is also shown as the dashed line in Figure 14a.

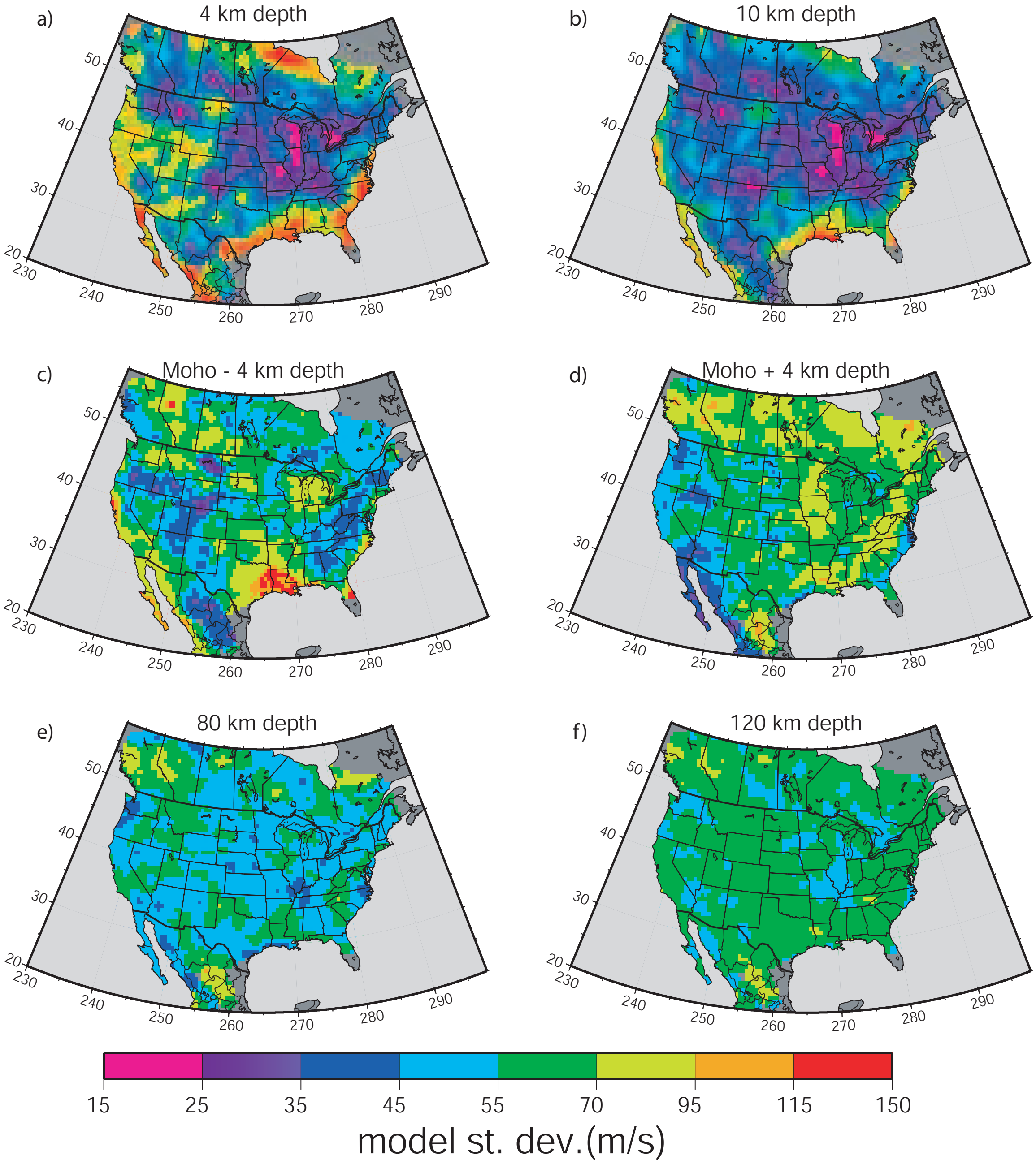

Figure 15. A selection of slices showing the computed standard deviation of Monte-Carlo models at the depths presented in Figure 11. Panels (c) and (d) show the results at 4 km above and below the Moho, respectively.

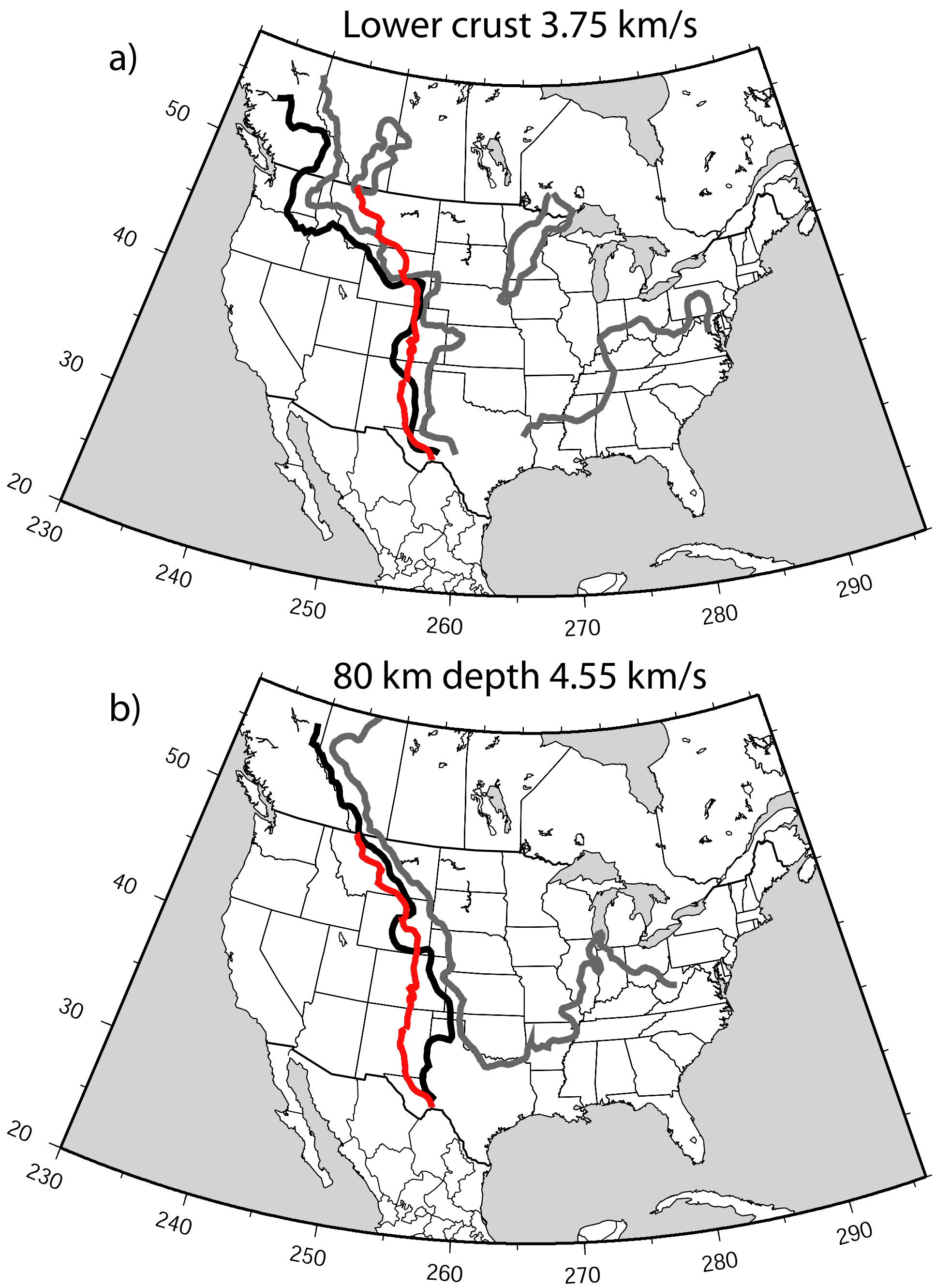

Figure 16. The location and uncertainty in the east-west velocity dichotomy for the lower crust (a) and the uppermost mantle (b). Contours of velocity are plotted for the 20th (grey) and 80th (black) percentile models at 3.75 km/s for the lower crust and 4.55 at 80 km in the mantle. The red contour marks the location of the Rocky Mountain Front.

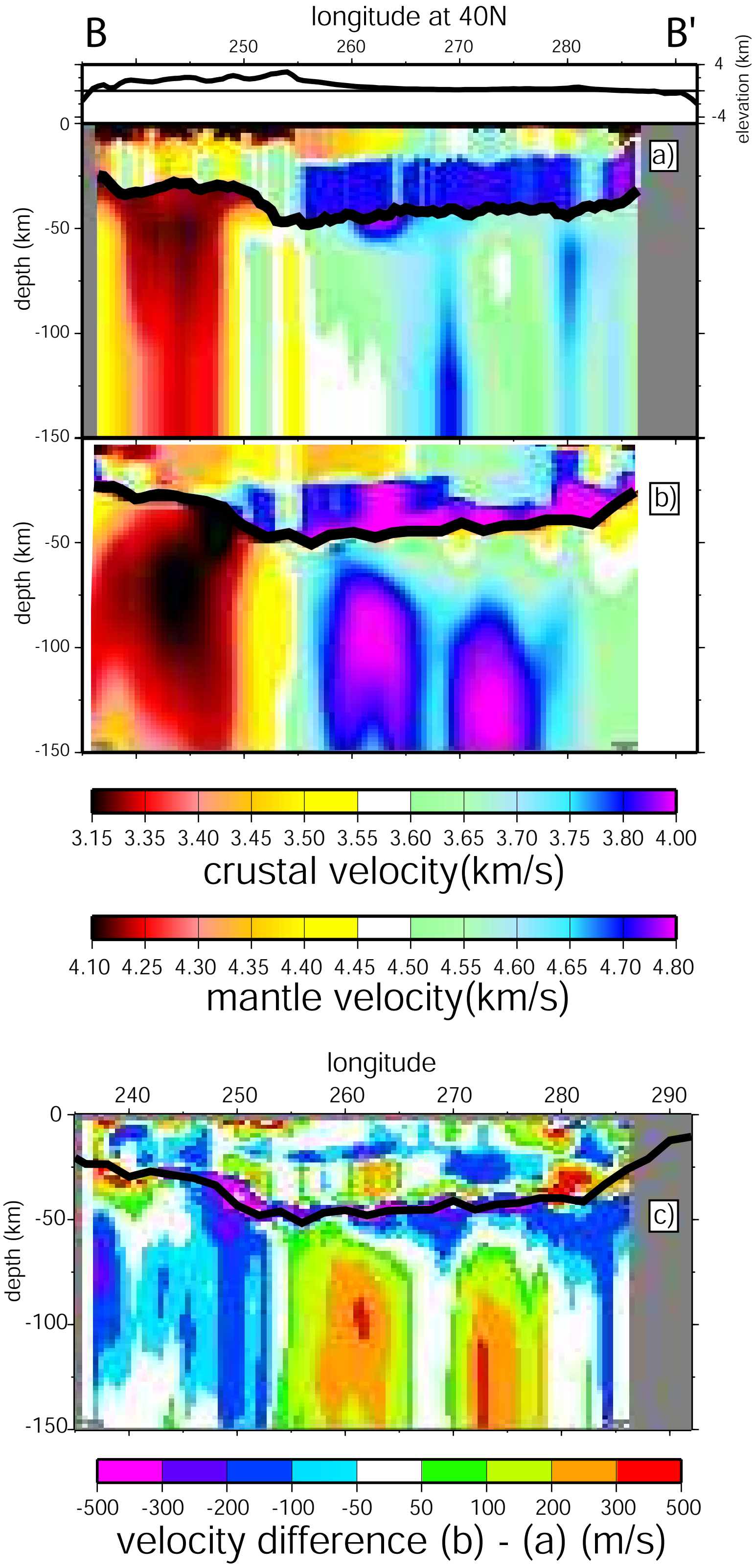

Figure 17. A comparison of our model (a) with that of *Shapiro and Ritzwoller* [2002] (b) at 40°N (Profile B-B' in Figure 13a). As in Figure 13, different velocity scales are used in the crust and mantle. A smoothed topography profile is plotted at the top of (a) and the recovered Moho from each investigation is over-plotted in (a) and (b). The difference of the two is shown in (c) as (b) minus (a) with the recovered Moho of (b) overplotted.

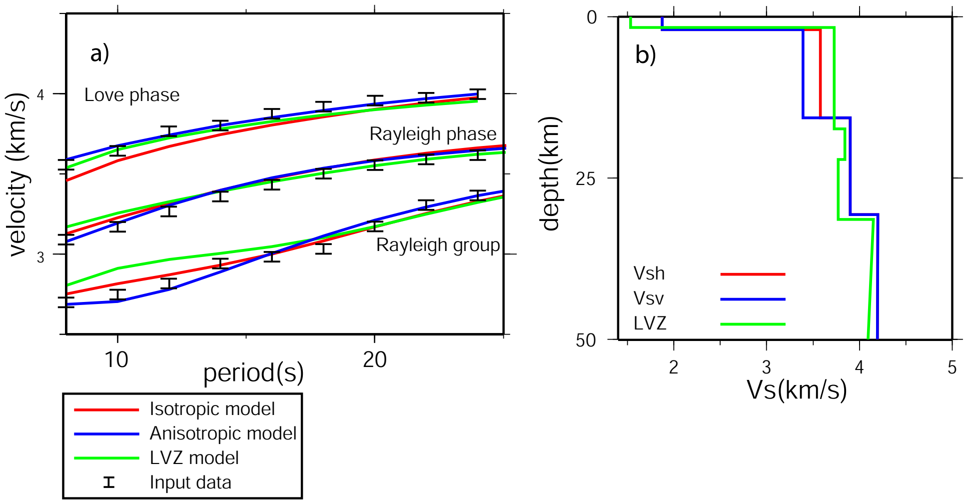

Figure 18. An example of the improvement in fit afforded by allowing radial anisotropy and low velocity zones (LVZ) in the crust. The dispersion curves for the isotropic, radial anisotropic, and LVZ are labeled in (a) and the corresponding model is shown in (b).

Table 1. Improvement in χ^2 values attained in a region of Nevada where radial anisotropy is found to improve data fit. Column 1 lists the method of crustal model parameterization used where 'Monotonic Isotropic' uses 3 crustal layers of monotonically increasing isotropic velocity, 'Non-monotonic Isotropic' is also isotropic but with the monotonicity constraint removed and using 4 crustal layers, and 'Radial Anisotropy' is where radial anisotropy was allowed in the middle or lower of the 3 crustal layers. Columns 2, 3 and 4 indicate χ^2 values for Love wave phase speed, Rayleigh wave phase speed and the average of the two. The final column lists the percent improvement over isotropic parameterization.

Param. type	χ^2-Love ph.	χ^2-Rayleigh ph.	χ^2-ave.	χ^2 % improvement
Monotonic Isotropic	2.21	1.42	1.81	
Non-monotonic Isotropic	1.45	1.63	1.54	15.2%
Radial Anisotropy	1.05	1.07	1.06	41.6%

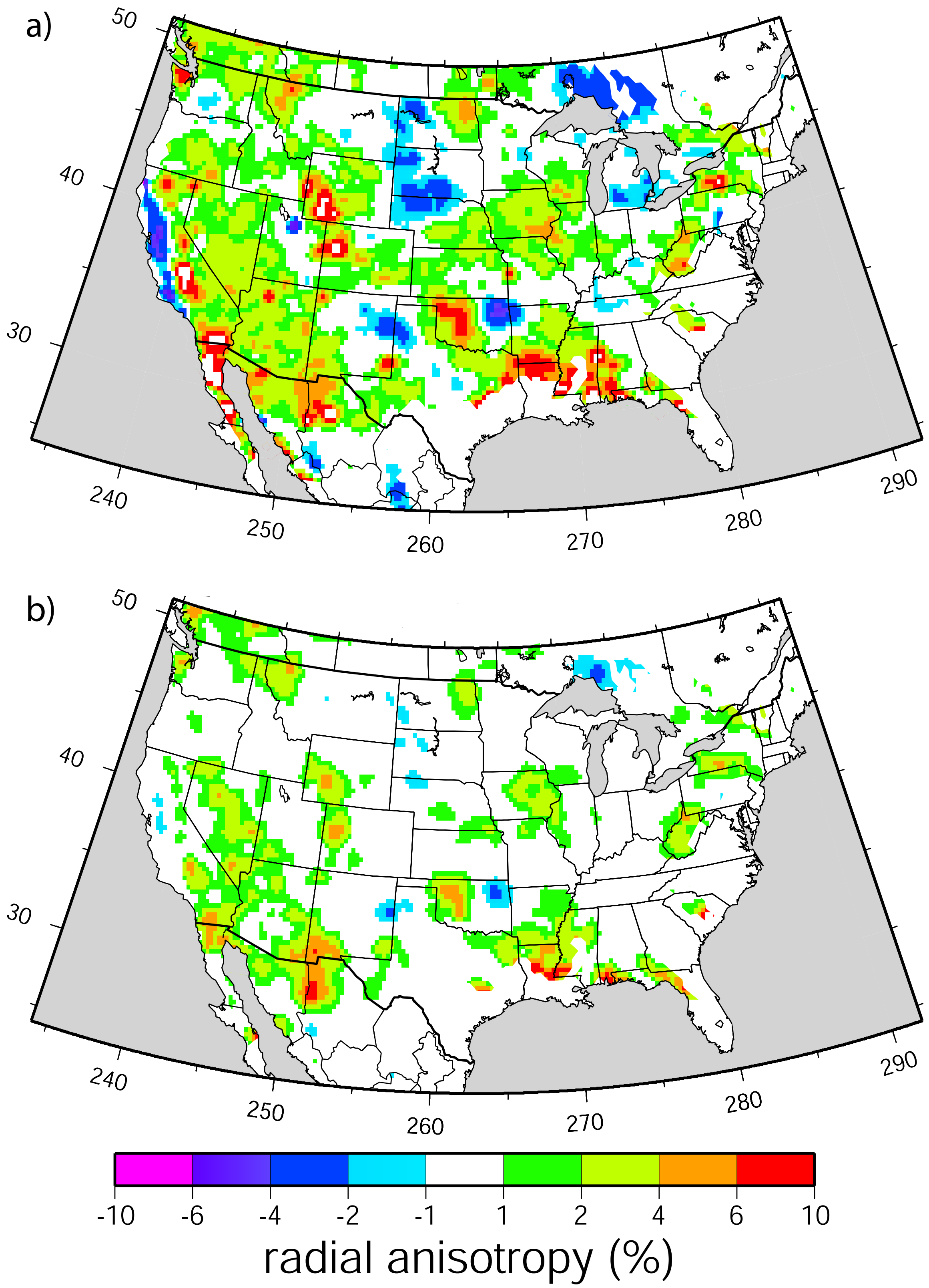

Figure 19. The favored crustal radial anisotropy results for the US where a value of 5% signifies $Vsh/Vsv = 1.05$. We report the values for the least anisotropic model from the ensemble of Monte-Carlo results.